INL/RPT-23-74062

Initial Fracture Propagation Modeling of Graphite Components with Grizzly

June 2023

B. W. Spencer[1]
L. B. Munday[1]
G. Singh[1]
V. Prithivirajan[1]

[1]Idaho National Laboratory

INL is a U.S. Department of Energy National Laboratory
operated by Batelle Energy Alliance, LLC

INL/RPT-23-74062

Initial Fracture Propagation Modeling of Graphite Components with Grizzly

B. W. Spencer[1]

L. B. Munday[1]

G. Singh[1]

V. Prithivirajan[1]

[1]**Idaho National Laboratory**

June 2023

Idaho National Laboratory
Computational Mechanics and Materials
Idaho Falls, Idaho 83415

http://www.inl.gov

Prepared for the
U.S. Department of Energy
Office of Nuclear Energy
Under DOE Idaho Operations Office
Contract DE-AC07-05ID14517

Page intentionally left blank

ABSTRACT

Graphite has historically been extensively used in power reactor cores and will be used in multiple types of advanced reactors currently under development. These graphite structural components can experience significant stresses due to nonuniform volumetric strains induced by irradiation and thermal expansion, which can lead to fracture. Robust tools for predicting fracture initiation and propagation in graphite structural components in nuclear reactors are important for evaluating component integrity, developing design standards, and interpreting experimental results to characterize graphite performance. The U.S. Department of Energy's Nuclear Energy Advanced Modeling and Simulation program has been developing degradation models for other structural components in nuclear reactors within the Grizzly and BlackBear codes. This report documents an effort to develop initial capabilities for modeling graphite fracture within these codes, building on prior efforts to model fracture in other materials. Major elements of this effort include developing a new system for modeling fracture nucleation and growth in two dimensions using the extended finite element method and incorporating a damage and plasticity model. These capabilities are applied here to model a representative graphite component and a splitting disc experiment used to obtain tensile strength.

CONTENTS

1 INTRODUCTION

Graphite has been employed as a neutron moderator, reflector, and shield since the development of the first artificial nuclear reactors. It has been used extensively in reactors used for power generation, including in the Magnox and advanced gas reactor (AGR) designs in the United Kingdom and Fort St Vrain high-temperature gas reactor (HTGR) in the United States, and the high-power channel reactor (RBMK) designed in the Soviet Union. There is operational experience for graphite exposed to molten-salt coolant from experiments, such as the Molten Salt Reactor Experiment (MSRE). Graphite is an important material for in-core components in the multiple types of advanced reactors under development in the United States, including molten-salt reactors, HTGRs, fluoride-salt-cooled high-temperature reactors (FHRs), and various microreactors. These components must be designed to ensure that integrity is maintained during reactor operation. Environmental conditions that can challenge graphite during normal operation include exposure to high temperatures, radiation, stress, and coolant, which could be an inert gas or molten salt depending on the reactor type. Depending on the reactor design, graphite could also be exposed to oxygen during normal operation or off-normal events. There is a significant need to understand and predict graphite behavior in the environmental conditions that will be experienced in the variety of advanced reactor applications currently being considered.

The effort documented here specifically focuses on the mechanical behavior of graphite in-core components. While these components generally don't carry significant loads, they can experience significant stresses due to nonuniform volumetric strains induced by irradiation and thermal expansion. These stresses can lead to fracture, which is generally the primary failure mode of concern for these components. The American Society of Mechanical Engineers (ASME) Boiler & Pressure Vessel Code [1] has provisions for the design of graphite core components in high-temperature reactors to avoid fracture. These code provisions provide well-defined processes that, when followed in the design of reactor components, are intended to keep the probability of fracture below acceptable limits.

Despite the fact that the ASME code is intended to prevent fracture initiation, there are multiple needs for computational capabilities to predict the initiation and growth of fractures in nuclear graphite components. Graphite is a complex material with a heterogeneous structure, and some amount of microcracking is expected to occur, even under conditions when macroscopic fracture is not expected. The design code provisions are still under active development and being able to predict fracture evolution is essential for developing procedures to prevent its occurrence. Similarly, it is important for those who are designing and assessing reactors to have tools to predict how fracture would propagate in core components if conditions more extreme than those anticipated in the design were to occur. The formation of fractures may or may not be a safety concern depending on the geometry of a given component, the role it plays, and the fracture locations. Another important role for fracture simulation tools is in interpreting experimental data. Multiple efforts are currently underway worldwide, including in the United States through the Department of Energy's (DOE's) Advanced Reactor Technologies (ART) program. When applied to these experiments, simulation tools can play an important role in understanding the physical phenomena occurring during the experiment, improving the usefulness of that data for design.

The DOE's Nuclear Energy Advanced Modeling and Simulation (NEAMS) program is supporting the development of simulation tools for a wide range of systems and phenomena in nuclear reactors, including nuclear fuel performance, reactor physics, thermal hydraulics, structural materials, chemistry, and coupling between these tools. The NEAMS-supported tools for structural component integrity are Grizzly and BlackBear [2]. Grizzly is an export-controlled code that contains models specifically targeted at nuclear reactor components, while BlackBear is an open-source subset of Grizzly. Both of these tools build on the Multiphysics Object-Oriented Simulation Environment (MOOSE) [3] and the physics modules that

are distributed together with MOOSE. These tools include previously developed capabilities for modeling fracture in light-water reactor pressure vessels, degradation of concrete structures, creep and creep fracture in alloy components in high-temperature environments. The capabilities described here are being integrated into Grizzly, BlackBear, and MOOSE, as appropriate, with general-purpose capabilities being integrated into the MOOSE modules as much as possible to facilitate code reuse for other applications.

While the present report documents the first efforts of the NEAMS program to develop simulation capabilities for graphite core components, this work builds on significant prior efforts to model fracture in the aforementioned other structural materials, as well as in ceramic nuclear fuel [4]. The present effort to develop simulation tools for graphite fracture complements other recent and ongoing efforts to simulate other aspects of graphite degradation. A recently concluded project funded by the U.S. Nuclear Regulatory Commission (NRC) developed models for oxygen transport and oxidation in graphite, as well as a post-processing tool for assessing component integrity using the ASME code provisions [5]. Both of these tools have been integrated into Grizzly. An NRC-supported follow-on project is developing simulation tools for other mechanisms of graphite degradation in the presence of molten salts. There is also ongoing work by the DOE's ART program to obtain experimental data on graphite mechanical properties and support development of the ASME code provisions for designing graphite nuclear reactor components. The NEAMS-supported work described here is being performed in coordination with these other programs and is intended to be complementary to that work.

In this report, we first summarize graphite mechanical properties and the current state of fracture modeling and assessments for graphite component integrity in Section 2. Next, we summarize the tools used here for fracture modeling, including their state prior to this effort and the enhancements made to those tools in Section 3. In Section 4, we simulate the behavior of tests used to obtain tensile strength using a nonlinear constitutive model. In Section 5, we describe typical graphite nuclear reactor component geometries and demonstrate the use of multiple methods to simulate the initiation and propagation of fractures in those components. Finally, in Section 6, we summarize the current effort and needs for future work in this area.

2 CURRENT STATE OF GRAPHITE FRACTURE ASSESSMENT AND MODELING

2.1 Properties of Graphite and In-Reactor Behavior

The synthetic graphite employed in nuclear reactor components is a composite polycrystalline material consisting of filler particles and pitch binder [6]. The properties of graphite are strongly influenced by its microstructural characteristics. Early nuclear graphites had large (>1.5 mm) grains and were anisotropic, while newer grades can have grain sizes as small as 20 μm and are nearly isotropic [7]. Grain size and characteristics can have significant effects on graphite engineering properties, and there is wide variation in the properties of these various grades. Various processes can be used in forming graphite, including extruding, molding, vibromolding, and isostatic pressing. Extruded grades tend to have properties that are more anisotropic than for other processes.

Table 1 shows some key structural graphite grades of interest for in-core applications, along with some basic information about those grades. This set of grades is by no means exhaustive, as there are many graphite grades that have been used or are available for nuclear applications. The grades included here include those for which data is being collected under the ART program, those that have been used in Western reactors for which data may be available, and those that U.S. advanced reactor vendors have committed to use in their designs. The objective of the present effort is to ultimately provide predictive models that can support U.S. advanced reactor vendors. To that end, there is interest in both grades being considered in those designs, as well as in grades for historical reactors or reactors no longer being built because data may be available to support model validation. Graphite grades are sorted here by grain size, and the types are based on the designations based on grain size in ASTM D8075-16 [8]. Models for some properties of some of these grades have already been implemented in MOOSE-based codes [9] and are denoted in this table.

Table 1: Key structural graphite grades of interest for model development and validation in the present effort. Based on data from [10–12].

Grade	Type	Nominal Grain Size (μm)	Forming Process	Reactor Applications	ART Data	MOOSE Models
2114	superfine	13	Iso. Pressed		✓	
ET-10	superfine	15	Iso. Pressed	KP-FHR		
IG-110	superfine	20	Iso. Pressed		✓	✓
CGB	medium-fine	200	Extruded	MSRE		
Gilsocarbon	medium-fine	500	Molded	UK AGRs		
H-451	medium	500	Extruded	FSV HTGR		✓
NBG-17	medium-fine	800	Vibromolded		✓	
PCEA	medium-fine	800	Extruded		✓	
PGA	medium-fine	800	Extruded	UK Magnox		
NBG-18	medium-coarse	1600	Vibromolded		✓	

Abbreviations include KP-FHR: Kairos Power Fluoride-Salt-Cooled High Temperature Reactor, MSRE: Molten Salt Reactor Experiment, UK: United Kingdom, AGR: Advanced Gas Reactor, FSV: Fort St Vrain, HTGR: High-Temperature Gas Reactor

Graphite has an irregular microstructure with numerous defects, such as microcracks and pores. Its porosity varies by grade but is generally around 20%. Its production process introduces microcracks, and it does not deform plastically by moving dislocations, so any nonlinear deformation (i.e., beyond the elastic regime) incurs the growth of microcracks, which can coalesce and form macrocracks [13–15]. Its mechanical behavior has much in common with concrete, another quasibrittle material consisting of aggregates within a matrix, with its stress-strain curve exhibiting a broad, rounded peak in compression and nearly elastic

behavior prior to fracture in tension, which is characterized by softening behavior rather an an abrupt failure. In the reactor, graphite's properties can be affected by irradiation hardening and radiolytic oxidation. Neutron irradiation introduces defects in the crystal lattice, which result in dimensional changes and increasing the strength. Oxidation causes mass loss and an accompanying decrease in the strength of the graphite.

Structures built of quasibrittle materials are well known to have a size effect, in which the stress at failure in larger structures is smaller than that for smaller structures. This has been studied extensively for concrete and other similar materials [16]. There are two main causes of this size effect. The first of these is the inherent statistical variation of the material properties. In larger structures, the likelihood of a critical flaw being in a highly stressed region of the structure increases, leading to increased likelihood of failure. This behavior is characterized by weakest-link Weibull theory [17–19], which is based on structural failure occurring when the weakest point in the system fails. The second cause of size effect is the energy released in the fracture process zone ahead of a crack tip, and the decreasing influence that has on fracture propagation as the size of a structure and the pre-existing large cracks or notches it contains increases.

Graphite would reasonably be expected to exhibit this classical size-effect behavior, although the evidence for this is inconclusive, and this is an area of active research (e.g., [7]). As described in a survey article [20], a number of statistical models have been proposed to characterize graphite fracture. Experimental data quantifying size effects is limited and contradictory. Despite the challenges employing weakest-link Weibull theory to characterize size effects, Weibull theory is used extensively to characterize strength distributions in fracture tests of a given fixed size (e.g., [21]) and is employed in the theory that forms the basis for the ASME code procedures [22].

Because of the extensive microcracks and pores inherent in graphite's microstructure, it is impossible to completely prevent cracking. In a retrospective on the United Kingdom's experience with nuclear graphite, Metcalfe [15] discusses the distinction between benign defects in the graphite structure and larger cracks that may impair component function. Great efforts are taken to inspect graphite components prior to service to detect surface-breaking flaws, and procedures are followed in the design to prevent cracking. However, it is more useful to view failure due to cracking as a loss of design function, rather than the initiation and propagation of fractures. In some components, the presence of macroscopic cracks may not impede functions such as the moderation of neutrons, directing coolant flow, and permitting the movement of fuel and control rods. However, in other cases, cracks could be a significant concern. It has been well documented that significant cracking has occurred in AGR graphite core components. The potential effects of these fractures on safe operation has been carefully evaluated by operators and regulators, and in many cases, reactors have continued to be safely operated. The lessons learned from operational experience with AGRs will certainly be relevant to the design and operation of advanced reactors being developed, as these reactors will likely encounter similar issues.

2.2 ASME Code Design Methodologies

The provisions in the ASME Boiler & Pressure Vessel Code pertaining to core graphite structures are in Section III, Division 5, Subsection HH, Subpart A [1]. These provide procedures that, when followed by designers, are intended to keep the probability of fracture below acceptable limits. The code provides two options: a simplified assessment, which is based on allowable stresses, and a full assessment, which employs a probabilistic analysis based on the work of Hindley et al. [22, 23]. This is a brief summary of the full assessment procedure:

1. Fit a three-parameter Weibull distribution to a set of experimental data to characterize the variation in the tensile strength

2. Determine the structural reliability class of the component, which dictates the allowable probability of failure (POF), which can range from 10×10^{-4} to 10×10^{-2}, with more critical components having lower allowable POF

3. Perform a linear elastic finite element analysis of a component of interest, taking into account external loading and intrinsically generated stresses due to thermal expansion and irradiation-induced volume change

4. Compute a scalar equivalent stress for each integration point using a formula that accounts for the ratio of compressive to tensile strength

5. Compute a process zone volume, V_m, based on the critical stress intensity factor and mean tensile strength

6. Sort the integration points by equivalent stress in descending order, and truncate the list to exclude those with stresses below a threshold value

7. Evaluate a local probability of failure, χ_i, for each integration point, i, based on the local effective stress and Weibull distribution parameters for the strength

8. Assign the integration points into groups starting from the highest-stressed ones, forming a new group when the group volume exceeds V_m and when the difference between the maximum and minimum values of chi_i in a group exceeds $\Delta = 0.2$

9. Compute the probability of survival for each group

10. Compute the overall probability of survival of the component as the product of that for the individual groups

11. Compute the POF of the component as one minus the probability of survival for the component

12. Deem the component acceptable if the component's POF is below the acceptable value.

The above code procedure accounts for size effects, but the Δ criterion in grouping limits the extent to which the POF is increased for large regions of the component subjected to similar stresses. The ASME full assessment procedure was implemented in a Python script included in the Grizzly code distribution as part of the aforementioned NRC-funded effort at Idaho National Laboratory [5]. A similar capability was also developed by the DOE ART program [24].

2.3 Fracture Propagation Modeling

In many cases, graphite components in the reactor are subjected to relatively minimal external loads. However, exposure to the reactor environment causes intrinsically generated stresses due to oxidation, thermal gradients, and irradiation-induced dimensional change that can be significant. Modeling fracture initiation and propagation in graphite components requires capturing these effects, as summarized in a recent review paper [25] by Arregui-Mena et al. in which the authors have presented a wide perspective on finite element studies conducted since the early 1970s using different commercial, noncommercial, general, and graphite-specialized codes. These phenomena are driven by multiple physics (e.g., heat transfer and radiation transport). In many cases, one-way coupling from other physics models to the mechanical models used to represent fracture is sufficient.

Similar to other components and materials, a variety of fracture mechanics methods are applicable to graphite fracture. For component-scale fracture modeling, most of the published work in this area employs continuum damage mechanics (CDM) or the extended finite element method (XFEM), or closely related methods, because of their computational efficiency. Much of the published literature on simulating graphite components is from various groups in the the United Kingdom, targeting AGR components. Early AGR simulations employed CDM [26] to model strength tests of an AGR reflector brick with a slice removed and mechanical loading applied, resulting in fracture in the root of a keyway. Later simulations of this same type of test were performed using XFEM [27, 28] and configurational mechanics, which similar to XFEM models discrete, mesh-independent fractures [29–31]. Later work simulating this test with XFEM included dynamic effects and cohesive tractions [32].

Zou et al. [33] proposed a continuum damage mechanics model that related the fracture surface traction forces with the displacements. This model used stress-based criterion for crack initiation and fracture-mechanics-based criterion (involving fracture energy) for crack propagation. A damage surface was used for damage evolution in a similar way to how the yield surface is used for the evolution of plasticity. The model was implemented in the commercial finite element code Abaqus using its user element subroutine and was applied for modeling fracture in L-shaped and channel-section graphite specimens. The fracture predictions were compared with the experimental data and were found to be in good agreement. This technique was later used by the authors [26] to model fracture in AGR bricks. The study also investigated the effects of methane holes in the brick on its failure. The approach used in these two studies relies on the prior knowledge of the crack initiation location since the analyst needs to insert the user elements in those mesh locations to model cracking.

Kyaw et al. [34] modeled fracture in a two dimensional (2D) representation of an AGR graphite brick under the effects of irradiation and radiolytic oxidation. Abaqus's XFEM modeling capability was used to model the fracture. The Gilsocarbon graphite material models were implemented in Abaqus using its user material subroutine feature and the fracture was modeled using Abaqus' built-in XFEM fracture modeling capability. The damage was modeled using linear traction-separation law with maximum principal stress criterion used for crack initiation and strain energy release rate used for crack propagation. It was found that the crack initiated at the keyway fillet region and propagated inwards towards the inner edge of the brick. This study was followed by a more detailed study [35]. In this later study, the effect of temperature and neutron dose on the fracture characteristics was investigated. It was found that an increase in temperature or neutron dose sped up the crack initiation and propagation.

Component-scale simulations of graphite including intrinsically-generated stresses were considered using XFEM by Singh et al. [36, 37]. In this effort, a representative very-high-temperature reactor (VHTR) reflector block was modeled in 2D, with cracks permitted to nucleate and propagate on one half of the block. Spatially varying temperature and fluence fields were applied, driving thermal expansion and irradiation-induced contraction. The authors used Abaqus' XFEM capability to model the fracture. The analysis involved the Monte Carlo approach: 30 models of the VHTR brick were generated with each brick having a unique set of strength and fracture toughness values generated assuming Weibull distribution. The graphite models were implemented in Abaqus using its user material subroutine, and the computed stresses were verified through a comparison with an analytical solution for a simple geometry. The maximum principal stress criterion was used for crack initiation, and damage evolution law was based on the critical fracture energy and a linear softening law. This analysis demonstrated the capability for crack initiation and propagation in a graphite brick. The failure probability of the brick was calculated as the fraction of the brick models for which the crack, which initiated on the outer edge, closely approached the control channel. Several cracks stopped after propagating some distance towards the control rod channel. Some of the simulations did not complete due to difficulties with numerical convergence.

Crump et al. [32] presented an analysis of the fracture and fragmentation of graphite bricks performed using XFEM and cohesive zone modeling approach, which they call XCZM. The capability was implemented into Code_Aster, which was developed by Électricité de France, and used for modeling fragmentation in a 3D AGR brick. XFEM was used for modeling displacements at the crack tip, and cohesive zone modeling was used to represent the failure criterion. XCZM enabled modeling multiple cracks at the same time. An algorithm based on a supervisory macro, which was is based on state of the cracks (initiated, arrested, away from the boundary, or propagated a sufficient distance), managed the propagation of multiple cracks.

Another approach for modeling fracture in brittle materials has been presented by Kaczmarczyk et al. [29]. The authors utilized the global dissipation term in the form of Clausius-Duhem inequality for establishing the crack-front equilibrium and crack propagation direction. A crack tip elastic equilibrium condition, which balances the configurational forces on the crack tip with the resistance of material, is imposed and the mesh smoothing is continuously performed in a problem-dependent Lagrangian Eulerian formulation. The crack tips produced using this method are smooth compared to the crack tips produced by just element splitting. The crack propagation direction is determined based on the configurational force that maximizes the energy dissipation at the crack front [30]. The technique was implemented in the code framework named the mesh-oriented finite element method (MoFEM) [31, 38]. This approach avoids the need to add enrichment functions to the finite element shape functions and was demonstrated using the example of a keyway root crack initiation and propagation in an AGR brick. This MoFEM fracture modeling capability is limited to linear elastic materials.

3 GRAPHITE FRACTURE MODELING CAPABILITIES AND DEVELOPMENT IN MOOSE AND GRIZZLY

Over the course of MOOSE's development, multiple fracture modeling methods have been implemented in MOOSE, including smeared cracking (which can be considered a CDM method), cohesive zone models on element-element interfaces, XFEM, peridynamics, phase-field fracture methods, and element deletion. Of these methods, smeared cracking and XFEM are the most feasible for practical component-scale simulations because of their computational efficiency. Here, we describe the status of those two models and the development performed in the present effort. In addition, this section describes the development of a damaged plasticity model that we have applied to model graphite, as well as models for other aspects of graphite material behavior and MOOSE convergence check improvements relevant to graphite component analysis.

3.1 Smeared Cracking Models

Smeared cracking models were among the earliest methods for accounting for fracture in finite element models, beginning with early work by Rashid on concrete structures [39] and ceramic nuclear fuel [40]. They represent fracture through the stress-strain models that capture constitutive behavior at integration points, so there is no need for computational machinery to track crack paths.

MOOSE has a smeared cracking model widely used in BISON simulations [4]. When the tensile strength is exceeded, an exponential softening law is used to soften the material in the direction normal to the first principal stress when the crack initiated. Similarly, a second and third crack are permitted to form in orthogonal directions. This is a fixed model because the crack directions are not permitted to rotate.

Softening models such as this one are notorious for making the global equation solution difficult. There is an option in the MOOSE smeared cracking model, which we employ here, that does not attempt to follow the softening curve in the stress calculation in the current step but rather uses the damage from the previous step. This is essentially an explicit integration of the damage, and its accuracy depends on the time step size. We control the time step in the calculations used here with this model to limit the damage increment, integrated over the volume of the model.

Smeared cracking models also tend to be mesh-dependent because the fracture energy dissipated depends on the element size. This can be mitigated to some extent by adjusting the area under the softening curve to match the material's fracture energy for a given element length. This works well if the fractures localize in a single band of elements, but fractures also sometimes poorly localize. A strategy that works well to address the latter issue, and which we employ here, is to spatially randomize the values of the tensile strength. The `VolumeWeightedWeibull` initial condition in MOOSE computes spatially randomized strengths for each element in a model based on the method described in [41], which adjusts the strengths of individual elements sampled from a Weibull distribution based on their volume.

3.2 MOOSE XFEM Capability Development

XFEM can represent arbitrary, mesh-independent discontinuities in an otherwise continuous finite element model. Originally applied for fracture modeling [42], XFEM can also model discontinuities, such as material interfaces. MOOSE employs the phantom-node method of Hansbo and Hansbo [43] to represent discontinuities in its XFEM implementation, which can be used to model nucleating and propagating

cracks [44], stationary cracks [45], and moving material interfaces [46]. Because it represents fractures as discrete entities, XFEM avoids many of the issues encountered by smeared cracking or other CDM models. MOOSE has an XFEM implementation, which was originally developed by a Laboratory Directed Research and Development project at Idaho National Laboratory from Fiscal Years 2013–2016.

The underlying algorithms to represent discontinuities in MOOSE's XFEM implementation are relatively mature in both 2D and 3D, but the methods to define crack locations are still under active development. This code, which is implemented in the XFEM module in MOOSE, has a modular structure that permits crack locations (or other discontinuities) to be defined a number of different ways using code objects that compute the intersections between cutting planes and finite elements. A number of options are available for defining cutting planes based on geometry and level sets. For propagating fractures, especially when there are multiple fractures, we believe the most straightforward way to represent evolving crack geometries is to use lower-dimensional meshes to define the crack planes. The initial implementation of fracture propagation in MOOSE, which is still an option, was limited to 2D and used an ad hoc method that initiated and propagated cracks based on the stresses on free surfaces, where new cracks were allowed to nucleate, or in the interior of the model domain, where cracks were permitted to advance through a single element ahead of an existing crack tip. While this approach has been successfully applied to model fracture propagation, it is sensitive to mesh size because of the stress concentrations at the crack tip, and crack paths can be very noisy due to local variations in the stress field.

To improve the ability to propagate cracks with XFEM in MOOSE, a prior NEAMS-supported effort developed a capability to propagate cracks in 3D, using a 2D cutting surface mesh defined in a 3D domain [47]. This capability interfaces with the fracture integral capability in MOOSE's TensorMechanics module and advances cracks when a criterion based on stress intensity factors is reached. This propagates cracks with smooth paths that don't suffer from the noise expected from local approaches. Jiang, Spencer, and Dolbow [44] used a 2D analog of that approach, but the code for that was developed prior to the fracture domain integrals currently available in MOOSE and was never merged into the main MOOSE codebase because of deficiencies in the architecture. Prior to the present work, there was a need for a robust method for 2D crack propagation in MOOSE analogous to its 3D implementation.

XFEM is an important tool for modeling fracture in graphite components, and to improve the ability of the MOOSE XFEM implementation to do that, we implemented an algorithm to define cutting planes in a 2D model based on a mesh with 1D elements in a 2D space, analogous to the aforementioned 3D capability that already exists in MOOSE. While the 3D capability is general, it is also complex and computationally expensive, so a 2D capability is important for simpler, efficient simulations of components that can be represented with 2D planar or axisymmetric models.

The basis of the current work is a 2D version of the UserObject that derives from `CrackFrontPointsProvider` and represents the geometric discontinuity through a separate lower dimensional cutter mesh. Previous work [47] implemented this capability for 3D simulations where a 2D triangulated cutter mesh represented the 2D crack face. The 3D mesh cutter capability is implemented as a MOOSE UserObject called `CrackMeshCut3DUserObject`. `CrackMeshCut3DUserObject` is able to evolve the 2D cutter mesh based on inputs from fracture integrals, capturing nonplanar brittle fracture or fatigue crack growth. The 2D mesh cutter capability called `MeshCut2DFractureUserObject` developed in our current work captures fracture in 2D solids under plane strain conditions by cutting the 2D finite element body with a 1D cutter mesh comprised of line segments. To capture nucleation, we implemented a `MeshCutRankTwoTensorNucleation` UserObject that will insert a minimum sized crack into the domain when a nucleation criterion is reached.

3.2.1 XFEM 2D Mesh Cutter and Example

The development of the 2D mesh cutter `MeshCut2DFractureUserObject` follows the same execution and communication patterns used by the `CrackMeshCut3DUserObject`. This includes communication between the various TensorMechanics module objects used for computing fracture integrals and the XFEM cutter UserObject representing and growing the fracture. The TensorMechanics objects needed for computing the fracture integrals are created by the `DomainIntegral` action. The `DomainIntegral` creates a `CrackFrontDefinition` used to describe geometric characteristics of the crack front for fracture integral calculations. For the XFEM mesh cutters, the `CrackFrontDefinition` communicates the crack geometry from the XFEM cutter mesh to the TensorMechanics fracture integrals. The `DomainIntegral` also creates an `InteractionIntegral` vectorPostprocessor for computing the various fracture mechanics parameters at a crack tip, such as $K_{I,II}$. The `InteractionIntegral` vectorPostprocessor communicates K values from the TensorMechanics fracture integrals to the XFEM mesh cutters. The XFEM mesh cutters then use the newly computed fracture integral values to determine if the crack propagates by checking if the following failure criterion is met:

$$K_c \leq |K| = \sqrt{K_I^2 + K_{II}^2} \tag{1}$$

where $|K|$ is a measure of K_I and K_{II}, the mode I and II stress intensity factors provided by the fracture integral, and the user-defined material property K_c is the critical stress intensity factor. The crack growth direction is given by the direction that maximized the crack-tip hoop stress, see Equation 5 in [44]. The crack propagates by a growth increment provided by the user. Quasistatic crack growth is assumed, and an iterative approach is taken to repeatedly solve the equilibrium equations, evaluate the fracture integrals, and as indicated by the failure criterion, incrementally advance the crack by a user-defined growth increment until the failure criterion is no longer met. To iteratively repeat the solution in this manner for each time step, `max_xfem_update` is set to 100 in the `Executioner` block. The `max_xfem_update` should be large enough to allow crack growth to cease during each time step. The XFEM cutter mesh can be output using a new `Outputs` object `XFEMCutMeshOutput`. This class outputs a new Exodus file at every time step with an extension that matches the convention used by MOOSE for other modified meshes (i.e., *.e-s0001, *.e-s0002)

The `MeshCut2DFractureUserObject` is demonstrated in the following regression test found at:
`moose/modules/xfem/test/tests/solid_mechanics_basic/edge_crack_2d_propagation_mhs.i`
The setup for this test is shown in Figure 1 where the FEM mesh being cut is shown in gray and the initial crack configuration used by the XFEM cutter mesh is shown in green. The bottom surface is held fixed and the two central nodes on the top surface are initially displaced by a fixed amount. The initial displacement and symmetry of the problem will cause both crack tips to extend and curve toward the top surface.

The initial displacement results in a $|K|$ at the crack tips that exceed K_c, and the crack is extended by a user-defined amount by inserting a line segment into the cutter mesh. This process is repeated for each xfem_step until the failure criterion is no longer met, $|K| \leq K_c$. The initial displacement applied in this problem requires three xfem_steps to reach an equilibrated configuration for the first time step, shown in Figure 2. The cutter mesh in Figure 2 was output using the `XFEMCutMeshOutput`. The three xfem_step resulted in three line segments being added to the end of each crack tip. The XFEM cutting algorithm modifies the finite element mesh by cutting it using the cutter mesh, resulting in the cracked simulation domain shown in Figure 3.

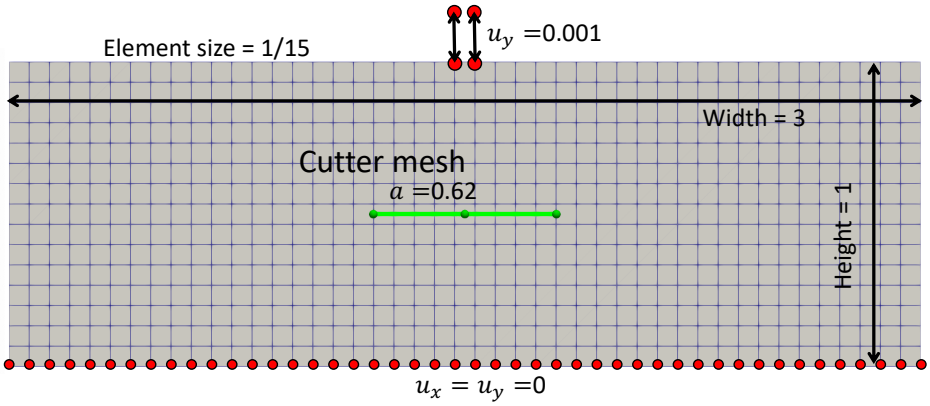

Figure 1: `MeshCut2DFractureUserObject` regression test setup, where the FEM mesh being cut is shown in gray and the initial cutter mesh is shown by the green line. The top two nodes shown in red are displaced, driving the crack extension.

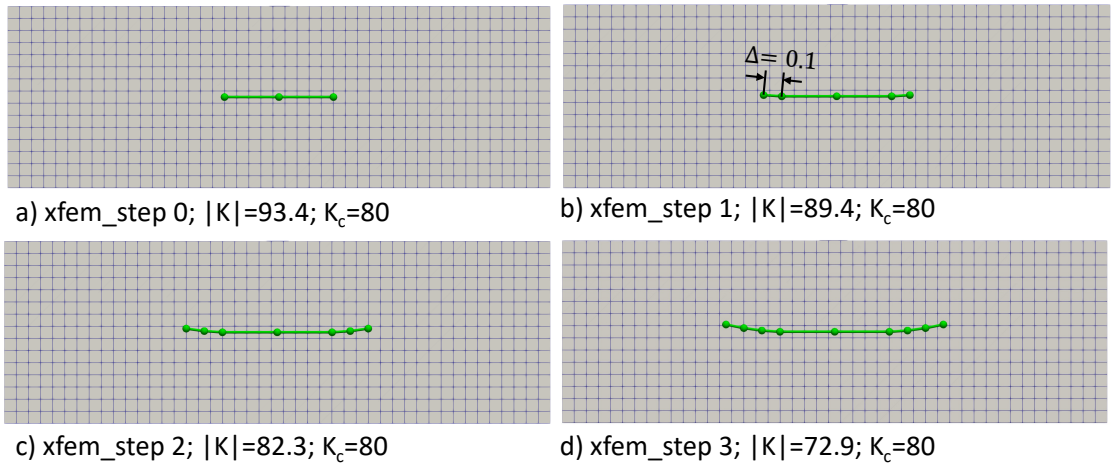

Figure 2: Crack growth of the XFEM cutter mesh shown at each xfem_step (a)–(d) during the first time step. $|K|$ and K_c are labeled for each xfem_step. Each xfem_step results in crack growth of $\Delta = 0.1$. (d) Final xfem_step for the first time step where crack growth stops when $|K| \leq K_c$.

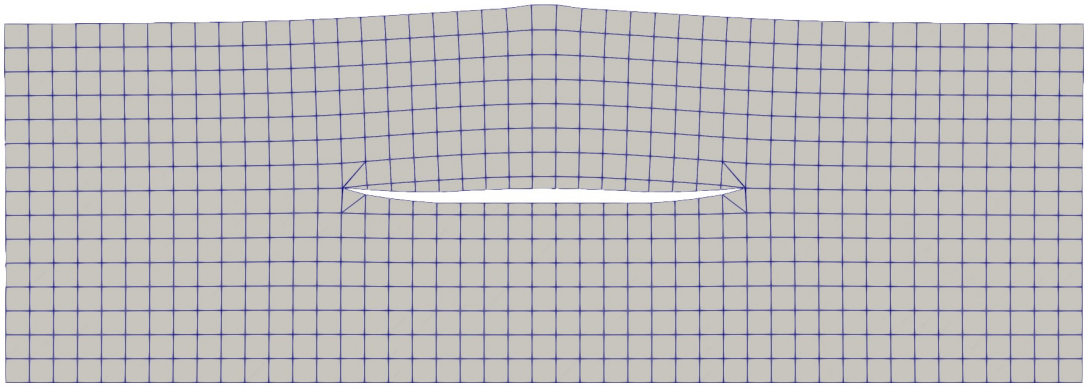

Figure 3: Final XFEM cut mesh after crack extension with 50× magnification of displacement field.

3.2.2 XFEM Nucleation UserObject and Example

The XFEM nucleation UserObject `MeshCutRankTwoTensorNucleation` inserts a crack into the cutter mesh used by `MeshCut2DFractureUserObject` when the nucleation criterion is met. The nucleation criterion is based on a scalar extracted from a specified `RankTwoTensor` (used to store stresses and strains in TensorMechanics), such as a principal stress or stress component. All of the standard scalar types that can be extracted from `RankTwoTensors` are available. For this work, we created a new scalar type for the nucleation criterion, `MaxInPlanePrincipal`, which excludes the out-of-plane component of the `RankTwoTensor` when computing the scalar. If the scalar exceeds a user-specified threshold, a line segment with a user-specified length is inserted into the `MeshCut2DFractureUserObject` cutter mesh. Cracks are only allowed to initiate from elements on user-specified boundaries. Once the nucleation criterion is reached, a line segment of the specified length is inserted into the cutter mesh, centered on the element centroid it nucleates from. The direction of the nucleated crack is normal to the direction returned by the `RankTwoTensor` scalar, for example, `MaxInPlanePrincipal` returns the direction of the maximum in-plane principal component and the crack direction is normal to this. The nucleation length should be at least the length of the element it nucleates in so that the nucleated crack will completely cut the element.

`MeshCutRankTwoTensorNucleation` copies several features available in the `XFEMRankTwoTensorMarkerUserObject`. These include the nucleation threshold being provided as a coupled variable and the computation of the maximum value of the scalar quantity used for nucleation. By providing the nucleation threshold as a coupled variable, it can be specified as either a constant or variable value. Coupled variable input is useful for introducing randomness in the strength by using an AuxVariable that has been initialized with a random initial condition, see the `VolumeWeightedWeibull` initial condition. The determination of crack nucleation is based either on the maximum value of the scalar quantity at all of the quadrature points in an element or their average value.

The `MeshCutRankTwoTensorNucleation` and its use in `MeshCut2DFractureUserObject` is demonstrated in the following regression test found at:
`moose/modules/xfem/test/tests/nucleation_uo/nucleate_edge_crack_2d.i`
This contrived test simulates two cracks being nucleated at different time steps and then being arrested before they reach the boundary. The setup for this test is shown in Figure 4 where the caption describes the simulation setup. The `MeshCut2DFractureUserObject` requires an initial mesh even if it is not used. This test is set up to capture crack nucleation, not the extension of a pre-existing crack, and a dummy cutter mesh is placed outside the structural domain, shown by the green line segments.

Simulation results are shown in Figure 5 where the model is first elastically deformed, followed by the nucleation of the cracks and crack growth. Note that a crack is first nucleated at $t = 3$ seconds in Figure 5(b) on the left side when the maximum principal stress reaches the nucleation_strength of 300 assigned as a coupled variable on the left side. A single line segment is inserted by the `MeshCutRankTwoTensorNucleation` and the stress intensity factor at this inserted crack tip is not large enough for the `MeshCut2DFractureUserObject` to extend the nucleated crack. A second crack is nucleated by the `MeshCutRankTwoTensorNucleation` on the right at $t = 4$ seconds in Figure 5(c) when the maximum principal stress exceeds the higher nucleation_strength on the right boundary of 400. The K stress intensity factor at the crack tip nucleated on the left is larger than K_c and the left crack extends. Due to the symmetry of the loading, the right crack that was just nucleated also has this same K value and so the `MeshCut2DFractureUserObject` extends the crack even though it was just nucleated by the `MeshCutRankTwoTensorNucleation` during this time step. As the top corners are further displaced at $t = 5$ seconds in Figure 5(d), both cracks extend by the same amount and are then arrested due to the compressive load in the center. The `MeshCut2DFractureUserObject` extends the cracks by three line segments, indicating three xfem_steps were taken during this time step. The simulation domain cut by the XFEM cutter and distorted by the displacement field is shown in Figure 6.

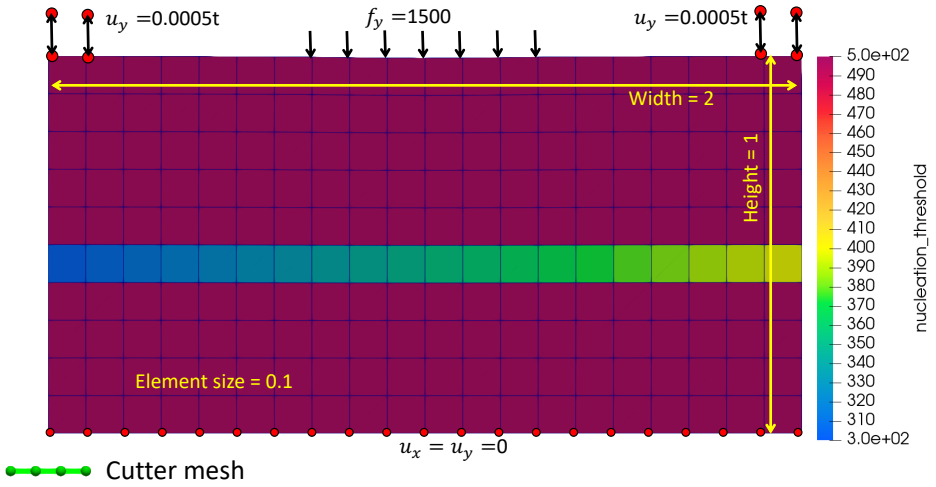

Figure 4: `MeshCut2DFractureUserObject` regression test set-up. The structural mesh is colored by the nucleation_strength field variable that consists of a weakened strip across the middle that ranges from 300 on the left side to 400 on the right. The boundary conditions are contrived to slowly nucleate and grow cracks from the left and right boundaries and then have the cracks arrested before they bisect the structure. FunctionDirichlet boundary conditions apply a time varying displacement on the top right and left corners to slowly build up the stress required to nucleate the cracks. A constant Neumann boundary condition is applied to the top center to produce a compressive stress field in the center that will arrest crack growth. The displacement is fixed on the bottom surface. A dummy cutter mesh is shown in green in the bottom left corner outside the structural domain.

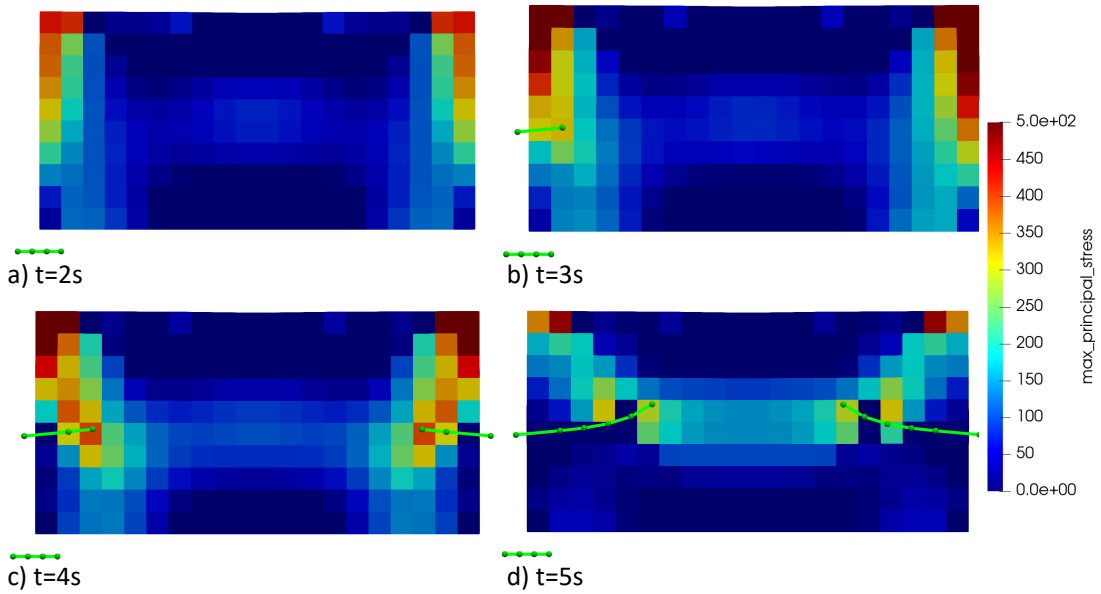

Figure 5: XFEM cutter mesh shown in green overlayed on finite element mesh colored by the maximum principal stress. (a) $t = 2$ seconds just prior to crack nucleation, (b) $t = 3$ seconds after the first crack is nucleated on the left when the maximum principal stress exceeds 300, (c) $t = 4$ seconds when the second crack nucleates on the right after the maximum principal stress exceeds 400, and (d) $t = 5$ seconds when the final configuration is reached and crack growth stops.

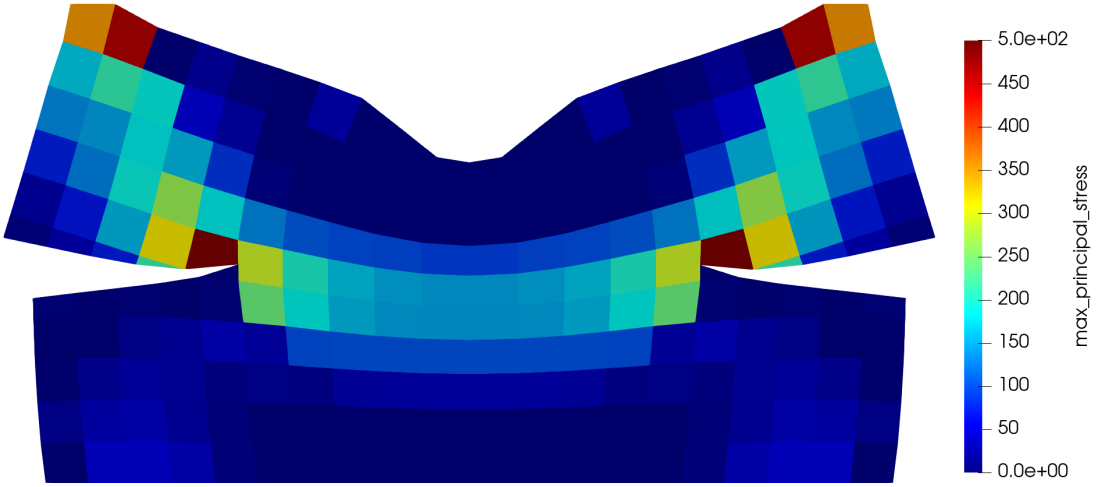

Figure 6: Final XFEM cut mesh after crack extension with 50× magnification of displacement field.

3.2.3 XFEM 2D Cutter Mesh and Nucleation Example: 2D Fuel Pellet

In this section, we demonstrate the `MeshCutRankTwoTensorNucleation` and `MeshCut2DFractureUserObject` on a large thermomechanical problem run in parallel to simulate the nucleation, growth, and arrest of several cracks over a long period of time. For this demonstration, we model the 2D fracture of a ceramic UO_2 nuclear fuel pellet under mixed-mode thermal and mechanical loading. This simulation attempts to reproduce results from Section 6.3.2 of [44] for the fuel pellet with an initial outer radius of 41 mm. This simulation is representative of fresh fuel subject to a ramp to full power. Thermal and mechanical properties for the UO_2 pellet are given in [44]. The element size used here is $h \approx 0.04$ mm, resulting in a mesh with 33,500 four-noded quadrilateral elements. Our mesh has slightly more elements than the 30,000 elements used by [44]. This work uses the same Weibull parameters as [44] for the nucleation strength shown in Figure 7, but randomness and element size will make the fields different. Our simulations use a constant $K_c = 2$ MPa$\sqrt{m}$ for crack propagation over the entire domain. The simulations by Jiang et al. use a random field for K_c with a mean value of $K_c = 2$ MPa$\sqrt{m}$ for the results shown in Figure 18 of [44]. Our simulations use a crack nucleation length of $a = 0.4$ mm; however, the `MeshCutRankTwoTensorNucleation` centers the nucleated cracks at the boundary element's centroid, leading to part of the nucleated crack being outside the domain. This results in our nucleation length being $a \approx 0.2$ mm, about half the nucleation length used in [44].

The cutter mesh is overlayed on the fuel pellet in Figure 8 colored by the maximum principal stress. The first crack nucleates in the element on the boundary with the lowest nucleation strength shown in Figure 7(b). The driving force is high enough to propagate the nucleated crack to the center of the fuel pellet where it is arrested due to the compressive stress in the center. The stress field is relaxed on the side where the first crack nucleates and the next cracks will nucleate from the opposite boundary where the stress reaches its highest values. This process continues, resulting in an almost symmetric profile of radial cracks in the pellet. The XFEM cut of the fuel pellet created by the crack causes a change in the heat transfer shown in Figure 9. The influence of cracking on the resulting temperature field is most apparent at the later times shown in Figure 9(c) and (d). Because it is assumed that no heat transfer occurs across the cracks in this model, discontinuities in the temperature field appear across the cracks when they deviate from being purely oriented in the radial direction.

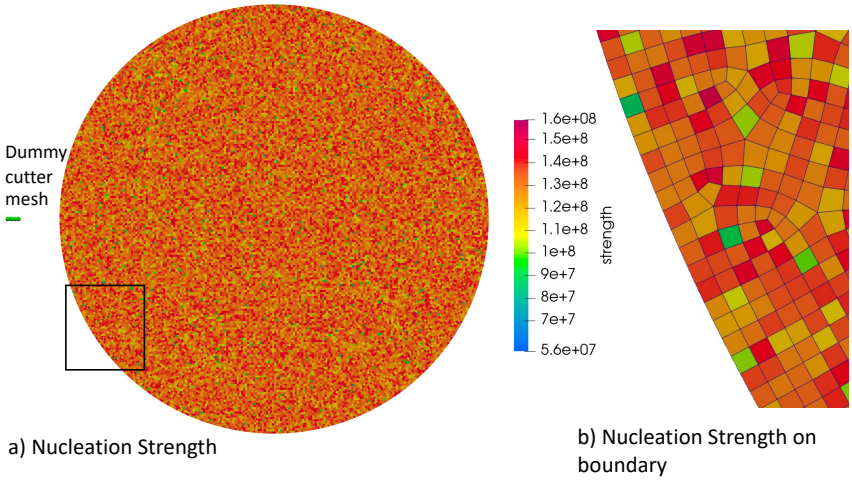

Figure 7: (a) Fuel pellet colored by the nucleation strength. (b) Close-up of the nucleation strength in the boxed region in (a) showing the range of nucleation strengths for elements along the boundary.

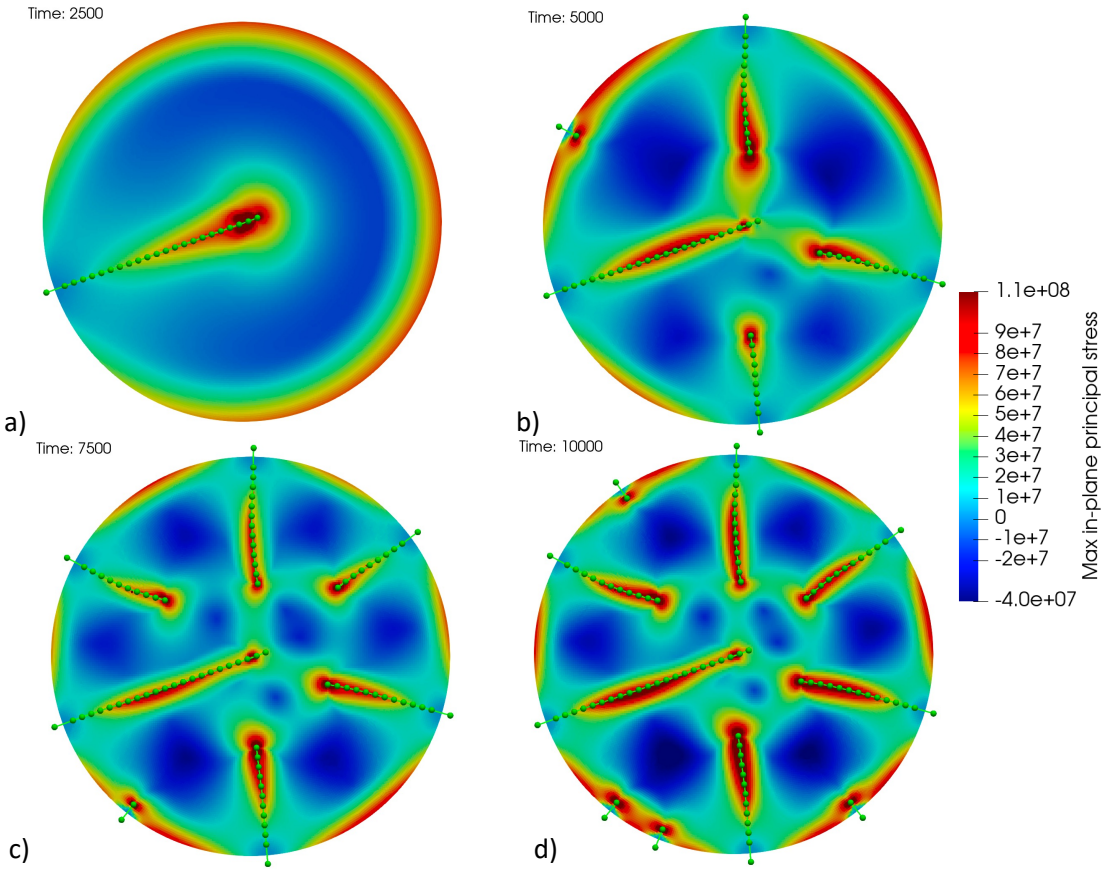

Figure 8: Cutter mesh shown by the green line segments overlayed on the fuel pellet mesh colored by the maximum in-plane principal stress. Time steps shown are the same as those presented in Figure 18 of [44].

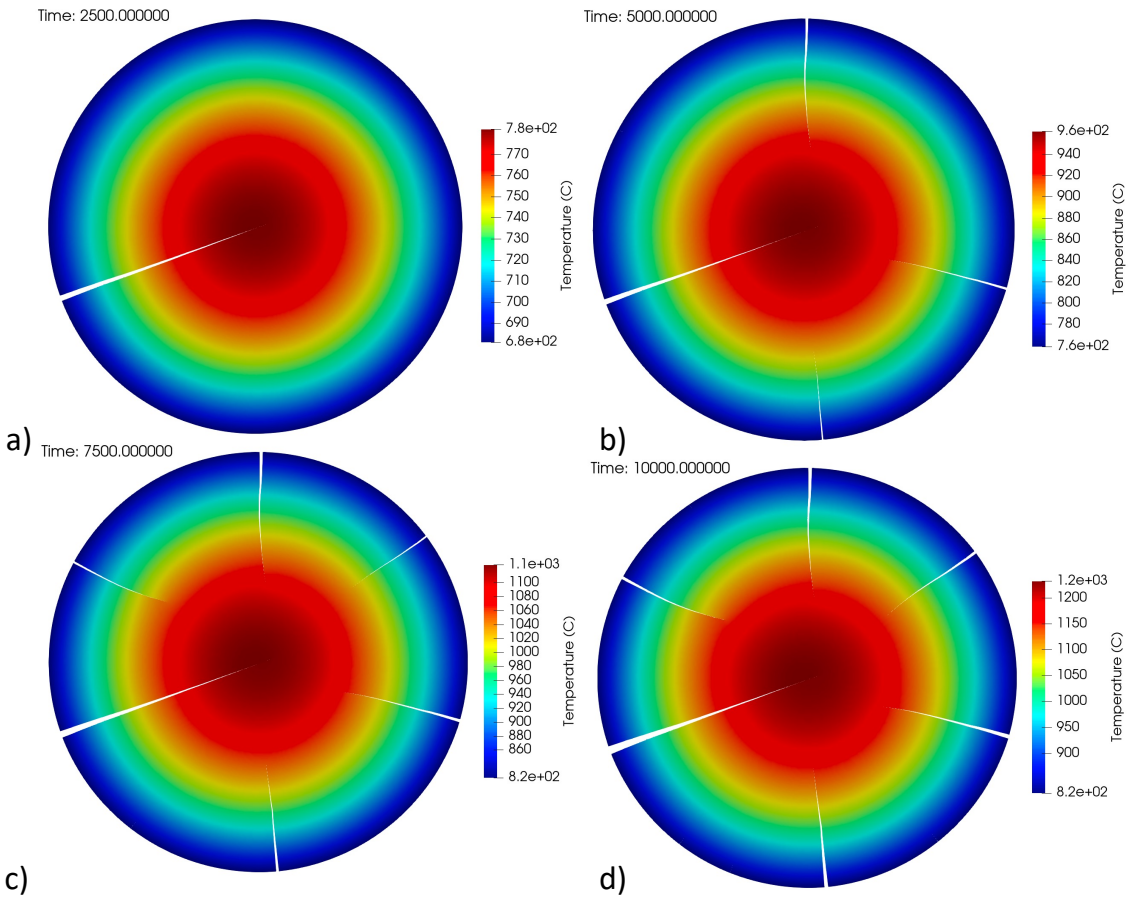

Figure 9: XFEM cut fuel pellet distorted by displacement field scaled by 5×. The fuel pellet is colored by the temperature field. Time steps shown are the same as those presented in Figure 18 of [44].

Our simulation shows straight radial cracks, which is more consistent with the results from Figure 19 of [44] that used a higher K_c of 4 MPa$\sqrt{m}$. This difference is likely due to our simulations using an initial nucleation crack size half that of [44]. Jiang, Spencer, and Dolbow [44] showed the effect of nucleated crack size on the fracture path in Figure 19 of their paper where smaller nucleated cracks resulted in cracks propagating radially toward the center while longer nucleated cracks resulted in curving cracks. Other causes could be the difference in Weibull distributions for the nucleation strength or constant versus random distribution for K_c. These simulations provide confidence that the XFEM nucleation and cutter mesh algorithms are nucleating cracks at the correct stress levels and those cracks are being propagated by the appropriate stress intensity factors.

3.2.4 XFEM 2D Cutter Mesh and Nucleation Future Work

In the previous section, we demonstrated the `MeshCutRankTwoTensorNucleation` and `MeshCut2DFractureUserObject` on a large-scale problem and were able to reproduce fracture patterns observed in literature [44]. Some future work for the 2D cutter mesh and nucleation UserObjects is to properly handle cracks near free surfaces and cracks that intersect. When a crack approaches a free surface, the nonlocal fracture integrals will begin to integrate over regions outside the mesh. This reduces the values computed by the fracture integrals, resulting in $|K|$ dropping below K_c, causing the cracks to arrest. This

can also occur when a crack is nucleated if the crack tip is located within the radius of influence of a free surface. To remedy this situation, one apprach would be to use local stress-based criteria to drive the crack in regions where the fracture integral approach is invalid, such as free surfaces and material interfaces.

Another issue observed in our simulations is the intersection of two growing cracks. In this case, the cracks do not interact with one another and pass right through each other. In reality, we would like the cracks to merge with one another. This capability would also likely enable the ability for the XFEM to handle crack branching.

3.3 Nonlinear Model for Compressive and Tensile Damage

While graphite exhibits quasibrittle behavior when loaded in tension, when loaded in compression, it shows a significant stiffness reduction prior to reaching the peak load. Its stress-strain behavior under uniaxial tension has a rounded peak [13, 14], which in many ways resembles that of concrete, another quasibrittle material. The mechanism for this nonlinearity is the formation of microcracks, rather than the movement of dislocations, as is the case for metals. To model the full behavior of graphite under a variety of loading scenarios, which might include compression as well as tension, it is important to have constitutive models that can capture that behavior.

Because of the strong resemblance of graphite's mechanical response to that of concrete, it is natural to look to existing models for nonlinear concrete behavior to model graphite. Two nonlinear concrete models had already been developed in BlackBear prior to this effort: the Mazars model [48, 49] and the Lee and Fenves model [50]. The Mazars model is a damage-mechanics-based model that captures nonlinearity in both tension and compression and uses a scalar damage index that decreases all components of the stress tensor to account for damage. It is attractive because of its simplicity and has been used widely. The Lee and Fenves model uses a combination of damage and plasticity models to more accurately capture the hysteretic cyclic behavior of concrete.

The Lee and Fenves model was previously implemented in BlackBear under a DOE Nuclear Energy University Programs project [51] but was never merged into the main codebase because it still needed additional code cleanup, testing, and documentation. Motivated by interest in using this model for graphite, we addressed those issues and merged this model into the main BlackBear codebase. This effort included a variety of improvements to the code quality, including improvements to naming conventions, adding Doxygen comments, and updating regression tests. We have applied this model in simulations of splitting disc tests, as described in Section 4.

While this model was successfully used here to capture nonlinear behavior in compression, it still needs further work to improve its robustness in capturing tensile failure. One effort that we undertook to enhance the versatility of the model and expand its applicability was to develop a hyperbolic Drucker-Prager plasticity potential as an alternative to the original version. This addition was motivated by the widespread use of this model in commercial software and its recognized accuracy in 3D simulations. We developed all aspects of this option for the model but are still in the process of testing and reviewing this before merging it into the main BlackBear code branch.

3.4 Thermal, Creep, and Volumetric Change Models for Graphite

In addition to the damage and fracture behavior, a comprehensive capability for graphite modeling requires models for thermal behavior, creep, and volumetric change due to temperature and irradiation. We have begun implementing these types of graphite material models in the Grizzly code. A prior effort focused

on carbonaceous fuel matrix materials in BISON [9] also implemented models for some structural graphite grades, and we used that effort as a starting point for a set of material models in Grizzly that will provide properties for a variety of structural graphite grades of interest.

We built on the prior efforts by adding missing properties for some graphite grades relevant to structural applications. These models, representing the properties for H-451 and IG-110 graphite grades, will be made available to the Grizzly users in the near future. Several properties in these models account for the anisotropy and include the dependence on temperature and neutron fluence. After incorporating models for H-451 and IG-110 graphite grades, we will survey available date on other relevant structural graphite grades and incorporate them into Grizzly as well.

3.5 Other Supporting Capability Development

A common feature of graphite components that affects their analysis is that they often have minimal external loading and are modeled as free bodies with unrestrained volumetric expansion or contraction. Appropriate boundary conditions must be applied for mechanical simulations of such bodies to prevent rigid body translation and rotation. These boundary conditions should be imposed in a way that imposes no constraint on the deformation of the bodies, and as a result, reaction loads at those boundaries should be essentially zero. This poses some unique challenges on the convergence criteria for the nonlinear solver, which we have helped address as part of this effort.

By default, MOOSE determines whether a nonlinear solution has converged by comparing the current residual to the initial residual for the current time step in a transient simulation. That can be problematic because, in some cases, the boundary conditions change only minimally, so the initial residual can be small. The `ReferenceResidualProblem` in MOOSE has long provided a solution to that issue by providing a way to compare the norm of the current residual vector to a reference vector, which typically consists of the vector of the forces on boundaries with Dirichlet boundary conditions. This is generally very effective but is problematic for unrestrained models, such as graphite components, because the reaction loads are small.

To address this issue, we collaborated with researchers at Los Alamos National Laboratory in developing a system to assemble a reference vector that consists of the absolute value of all contributions to the residual from the finite elements that contribute to the residual at a given degree of freedom. This vector provides a physically meaningful reference vector for determining relative convergence, which works well for all problems regardless of their boundary conditions. This capability was merged with our support, and we have used it successfully in the component simulations in Section 5, for which defining appropriate convergence tolerances was previously challenging.

4 FRACTURE TEST SPECIMEN DEMONSTRATIONS

The disc compression test, also known as the Brazilian test, is an important way to obtain the tensile strength of brittle and quasibrittle materials. In this test, a disc-shaped specimen made of the material of interest (graphite, in our study) is subjected to compression loading on opposing sides, as illustrated in Figure 10(a). This loading configuration induces a combination of tension and compression stresses within the disc, with the highest tensile stresses occurring at the center of the disc oriented along the loading direction. As the test progresses, the disc progressively splits into two halves along the center line aligned with the loading axis.

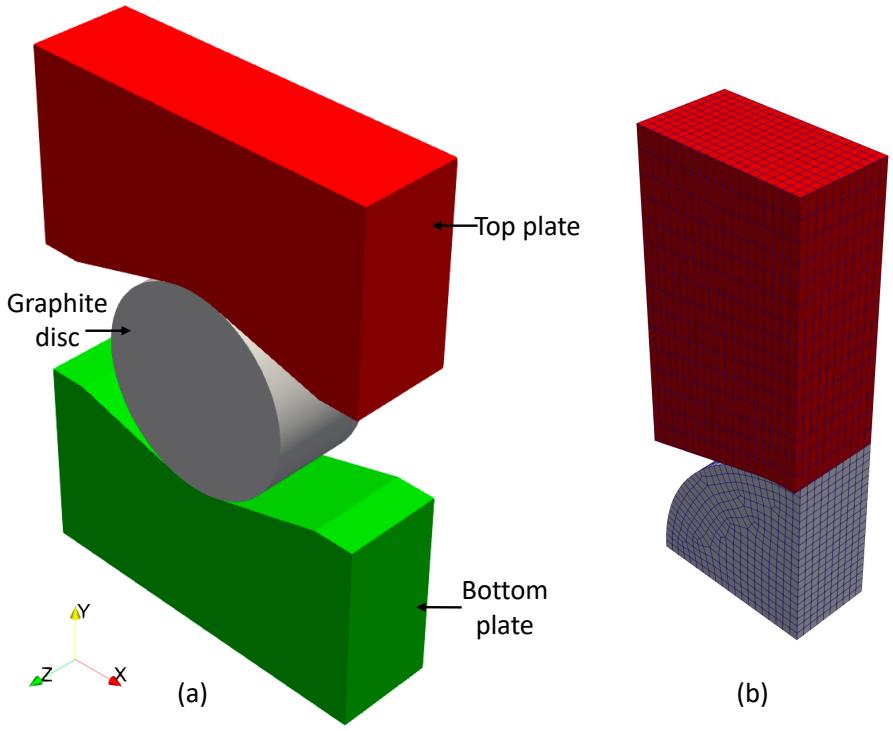

Figure 10: (a) 3D experimental setup of the splitting tension test and (b) 3D meshed model simplified by in-plane symmetry considerations.

While direct tension tests arguably provide a more defensible direct means to measure tensile strength [52], there are ASTM standards for using the disc compression test to obtain the tensile strength of graphite [53], as well as other materials such as concrete and rock. The major benefits to this test are that it is easy to perform and requires a minimal amount of material, which is important for testing irradiated graphite. The primary challenges with this test are that it is difficult to know the tensile stress that the material on the centerline is subjected to and that the material is subjected to complex multiaxial loading.

Because graphite experiences significant nonlinearity in compression, the stress state in a disc compression test could be significantly affected by material nonlinearity by the time the tensile strength is reached. The damaged plasticity model described previously is an ideal candidate for a model to capture that behavior to permit a better estimate of the stresses at failure and potentially improve the ability of the disc compression test to predict tensile strength.

We modeled this experiment using a simplified 3D model representing a quarter of the graphite disc and top steel plate as shown in Figure 10(b), taking advantage of symmetry planes. The dimensions of the

graphite disc used in the simulations (as well as experiments) have a diameter of 12.7 mm and a thickness of 6.35 mm.

For calibrating the damage plasticity model, we utilized experimental data of IG-110 graphite, which has not yet been published. Since these experimental curves have not been published yet, we are unable to include calibration plots in this report. The initial calibration process was based on uniaxial compression stress-strain curves. After the initial calibration, we performed simulations of the splitting tension test and analyzed the results. Although the model did not perfectly capture the peak load in the splitting tension simulation, which may require further calibration, our objective was to qualitatively assess whether the use of the damage plasticity model captures the expected behavior. This includes evaluating the distribution of stress in the disc and identifying the most likely location of failure indicated by the damage parameter.

It is important to highlight that we explicitly simulated the contact between the curved load plate and graphite disc, replicating the conditions observed in experimental testing. We used frictionless node-face contact enforcement here. Figure 11 shows the contact pressure on the disc resulting from the compressive load applied to the top of the plate.

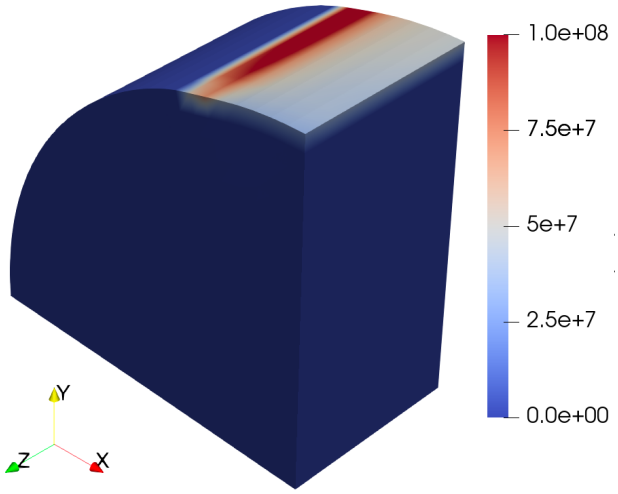

Figure 11: Contact pressure (in Pa) on the surface of the disc due to compression from the top plate.

The spatial distribution of the xx component of the stress tensor and the scalar damage variable obtained from the simulation are presented in Figure 12 (a) and (b), respectively. In Figure 12(a), we observe a stress distribution where tensile stress is concentrated towards the center line, while compressive stress is observed as we move away from it. This stress distribution is consistent with the past literature data and experimental observations, indicating that the model qualitatively captures the expected behavior.

Figure 12(b) shows the scalar damage variable, which reveals its highest value near the center of the disc. This indicates a high propensity for failure at that specific location. This qualitative agreement between the simulation results and expected failure location further demonstrates the model's capability to capture the relevant behavior.

Overall, the spatial distribution of the stress tensor and scalar damage variable obtained from the simulation align with the anticipated patterns based on previous studies and experiments, providing confidence in the model's ability to capture the essential aspects of the material behavior.

Finally, we conducted an additional simulation using a purely elastic model for the graphite disc to emphasize the significance of employing a nonlinear model like damage plasticity in capturing field quantities such as strain. This can be validated through experiments using digital image correlation. Figure 13 provides

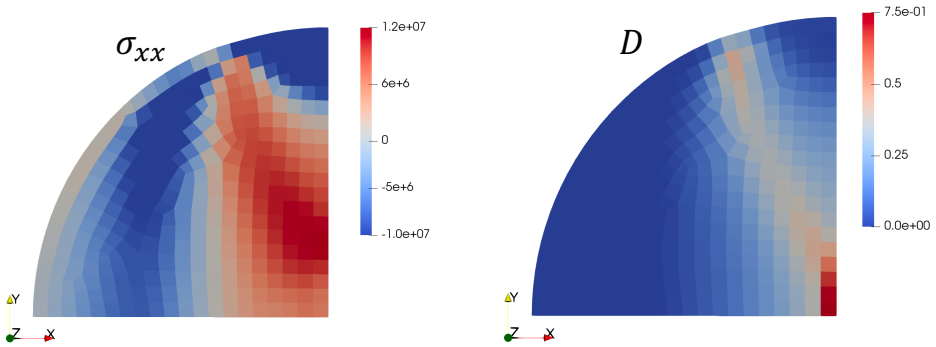

Figure 12: Spatial distribution of (a) xx component of stress and (b) scalar damage variable on the disc at peak load.

a comparison between the strain fields obtained from the damage plasticity simulations and the elastic simulations.

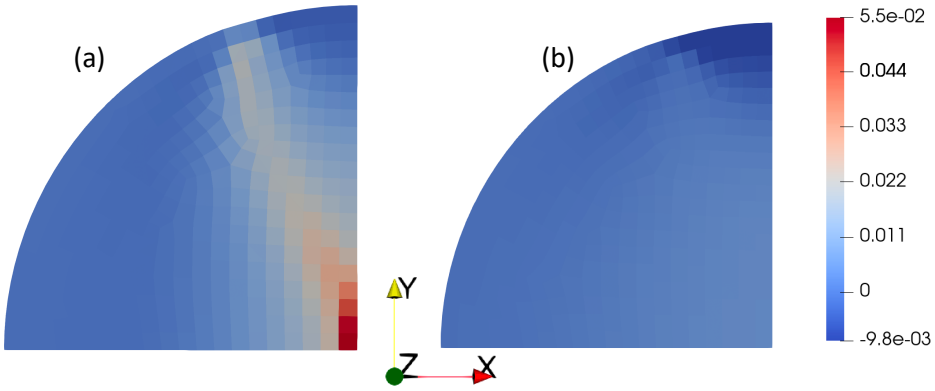

Figure 13: Difference in xx component of strain obtained from a (a) damage plasticity simulation and (b) elastic simulation.

As shown in Figure 13, there is a noticeable concentration of strain at the center of the disc in the damage plasticity simulations, which is expected due to the accumulation of damage. On the other hand, the elastic simulations fail to capture such localizations. To further illustrate the disparity, Figure 14 specifically compares the xx component of strain values along the x- and y-axes, corresponding to the center line of the disc. It is evident that the elastic model severely underestimates the strain when compared to the damage plasticity model for these load levels, with a maximum difference of approximately a factor of 10.

This comparison highlights the importance of utilizing a nonlinear model like damage plasticity to accurately capture the strain distribution, particularly in regions of high damage accumulation. The results emphasize the limitations of an elastic model in capturing the complex behavior observed in quasibrittle materials, such as graphite.

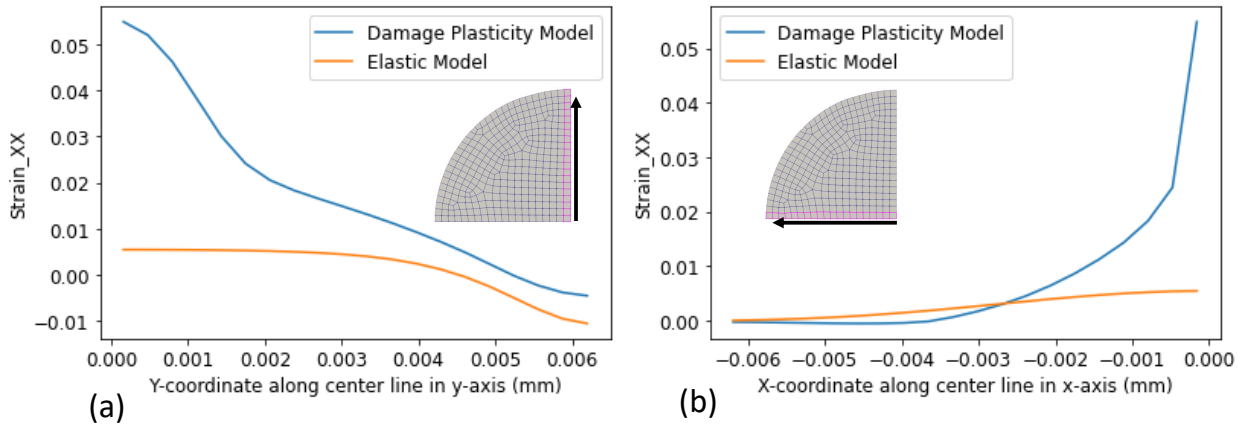

Figure 14: Comparing the xx component of strain obtained from damage plasticity model and elastic simulation along the center line in (a) y-axis and (b) x-axis.

5 GRAPHITE COMPONENT FRACTURE DEMONSTRATIONS

To demonstrate fracture initiation and propagation modeling in a graphite component, we employ here a model of a VHTR reflector brick. The VHTR is one of the six candidates of Generation IV nuclear systems in the technical roadmap of the Generation IV International Forum [54]. Electricity and hydrogen would be co-generated from a VHTR reactor. A VHTR is graphite moderated and helium cooled and has a high outlet temperature ($\approx$ 1000°C), which would allow hydrogen generation from water through a thermo- or electrochemical process. The VHTR concept is based on the existing HTGR and can have either a prismatic-block or pebble-bed core. The primary advantages include high thermal efficiency, inherent safety, process heat application capability, and modular construction [55].

5.1 Geometry and Finite Element Mesh

We have used both 2D and 3D models of the VHTR reflector brick in this application. The brick dimensions and its location in the core are shown in Figure 15. The meshes are shown in Figure 16. The 2D mesh consisted of about 11,000 elements while the 3D mesh had about 2,260,000 elements.

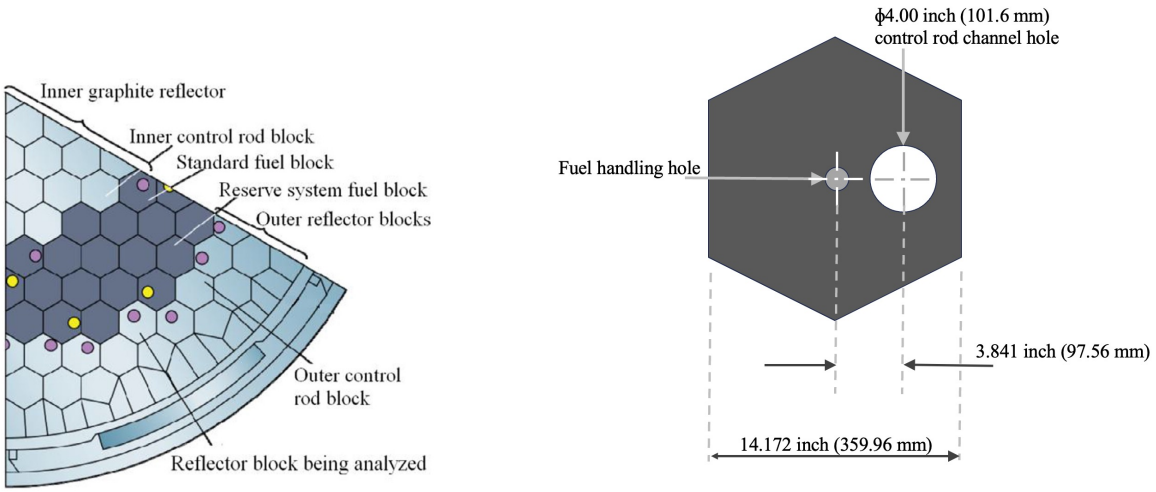

Figure 15: Location of the analyzed brick in the core and its dimensions, where the brick height is considered to be 31.22 inches (793.0 mm) [56].

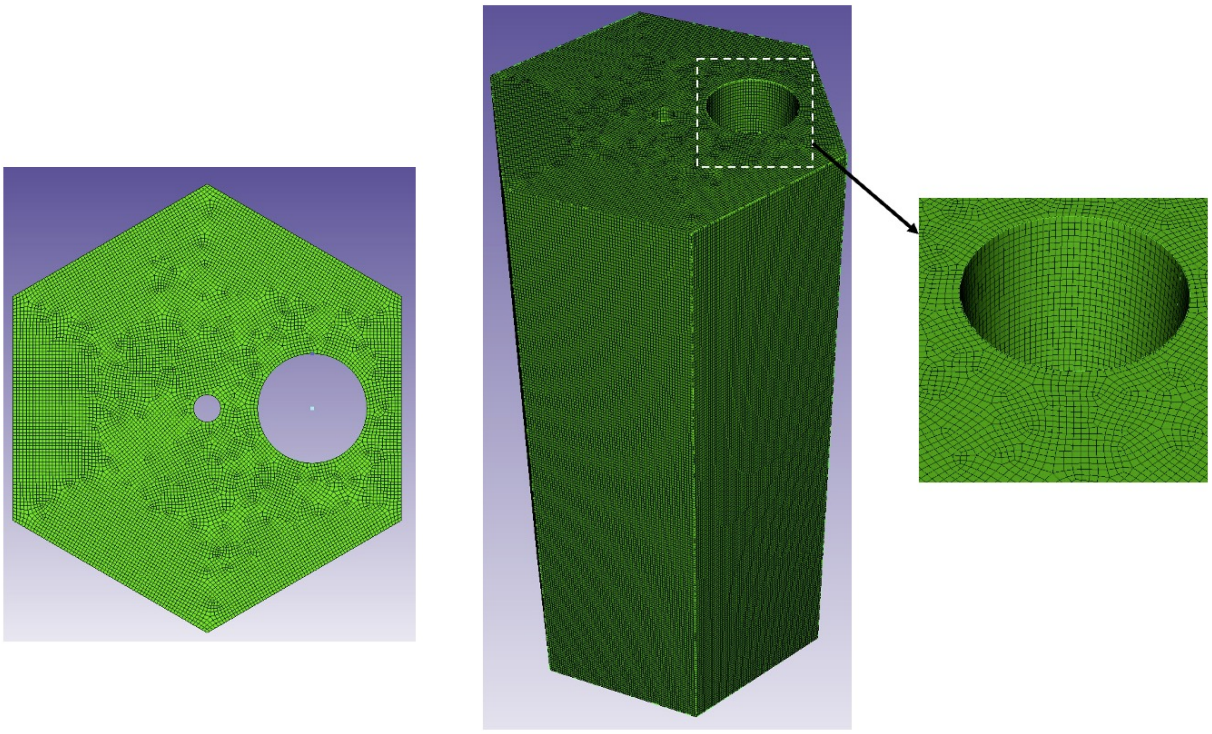

Figure 16: 2D and 3D finite element meshes of the VHTR reflector brick with an enlarged view of the control rod channel on the right.

5.2 Thermomechanical and Irradiation Properties

The properties of H-451 graphite grade were used for the analysis. The thermal properties are based on Reference [57]. The thermal expansion coefficient, elasticity properties, and the irradiation-induced dimensional change of graphite are functions of temperature and neutron fluence. These properties are based on the Graphite Design Handbook [58]. The Young's modulus is considered to be isotropic; an average of the Young's modulus in the radial and axial direction, as provided in the handbook, is considered for the analysis. The irradiation-induced creep is neutron fluence and temperature dependent and is computed according to Engle et al. [59].

5.3 Operating Conditions

The temperature distribution is prescribed and shown in Figure 17. The neutron fluence distribution takes into account the presence of fuel bricks located next to this reflector brick (see Figure 15) and shown in Figure 17. Both temperature distribution and neutron fluence are based on the information presented in Reference [56].

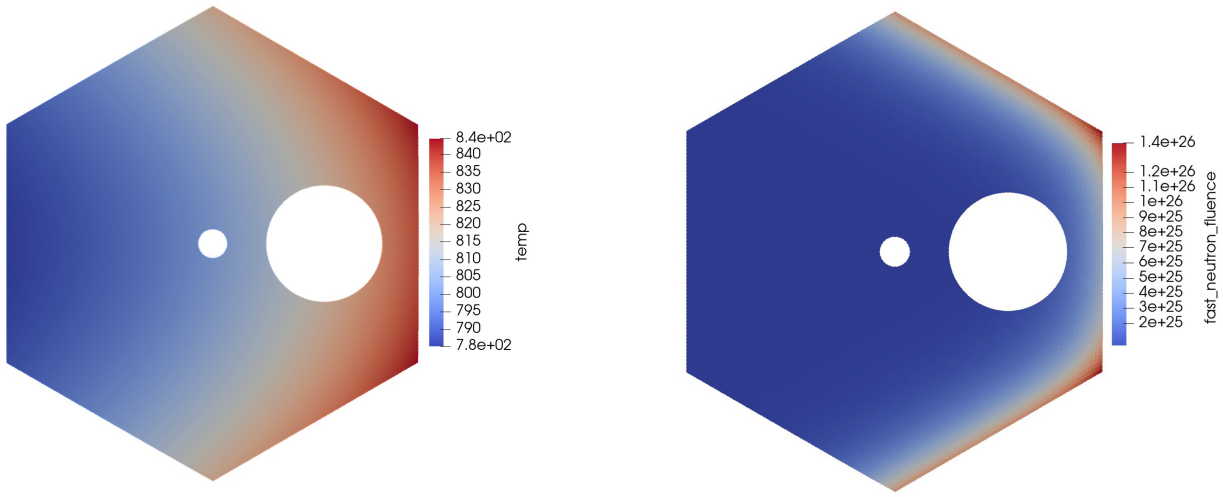

Figure 17: Temperature (K) and fluence distribution (n/m^2) in the graphite reflector brick [56]. Fluence shown is at the end of 30 years.

5.4 Fracture Model Parameters

We ran the 2D models using both smeared cracking and XFEM to represent fracture, while we ran the 3D model using the smeared cracking model. Both of the 2D models employed generalized plane strain, which assumes that the out-of-plane strain (in the z direction) is constant and computed so that the integral of the stress in that direction is zero. This permits unrestrained free expansion in that direction.

For all these models, we generated a randomized strength distribution using the `VolumeWeightedWeibull` initial condition. The two-parameter Weibull distribution was assumed to have a median of 15 MPa and a Weibull modulus of 10, based on the properties for H-451 graphite in [21]. These are properties derived from fracture coupon tests and were assumed to apply to the component scale, without scaling for size effect. We simply specified the reference volume to be approximately equal to the nominal element volume. The correct handling of size effect is an area for future research. Figure 18 shows the randomly generated strength distributions for the 2D and 3D models.

In the XFEM model, fractures are assumed to nucleate when the maximum in-plane principal stress exceeds the randomly sampled strength. Fractures were only permitted to nucleate in elements adjacent to a free surface to avoid issues with fractures interacting with each other. We assumed the length of nucleated cracks to be 10 mm. Based on data from [58], we assumed a value of 1.5 MPa$\sqrt{\text{m}}$ for the fracture toughness, K_{Ic}, as a threshold for crack growth. When crack growth was indicated, the cracks were incrementally extended by 2 mm, and the solution was repeated and fracture integrals re-evaluated until the mode-I stress intensity factor, K_I, was lower than K_{Ic}. The nominal mesh size is 3 mm, so the line segments created by propagating cracks will often not fully pass through an element.

For the smeared cracking model, we assumed the standard relationship between the critical energy release rate, G_c and K_{Ic}:

$$G_c = \frac{K_{IC}^2(1-\nu^2)}{E} \tag{2}$$

where E is the elastic modulus and ν is the Poisson's ratio. We selected parameters for the softening law so that the total area under the stress vs. displacement curve for a single element loaded in tension was equal to G_c. In the smeared cracking model, there is an option to specify the direction of the first crack, and we

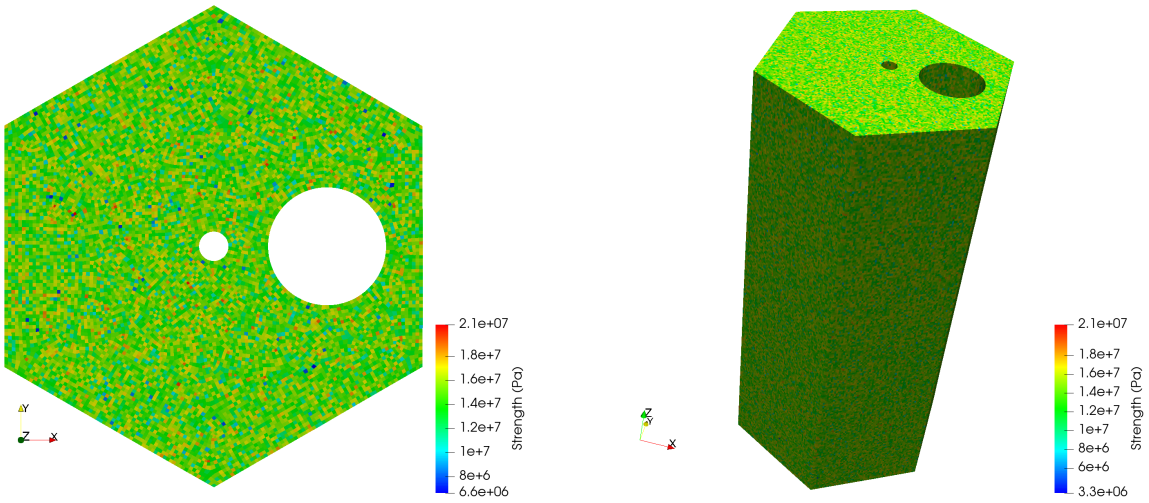

Figure 18: Randomly sampled tensile strength (Pa) for (left) the 2D models and (right) the 3D model.

specified it as the z direction to enable explicit tracking of out-of-plane cracks or cracks aligned in the plane normal to the axial dimension of the block. These cracks, referred to here as axial cracks, are modeled using the same softening law as is used here for in-plane cracks but should in general have parameters tuned for their behavior.

While the 2D XFEM model captures in-plane cracks, XFEM does not capture axial cracks. We represent these cracks here by using the smeared cracking model for softening only in the z direction, using the same parameters used in the model that used smeared cracking for in-plane cracks. We specified the crack direction and that only a single crack can form, preventing the smeared cracking model from modeling in-plane fracture.

For the smeared cracking models, to minimize errors introduced by using the damaged stiffness from the prior step, we limited the simulation time step such that the integral of the damage increment over the component volume was less than 5%. Testing indicated that there was little change in the solution when the step size was further limited, but further investigation is needed on the acceptable limits.

5.5 Results

The 2D planar models (XFEM and smeared cracking) and 3D models were all run for 30 years of exposure to the reactor environment. The fracture predicted by the 2D XFEM and smeared cracking models are compared at various times in terms of the in-plane fracture in Figure 19 and axial fracture in Figure 20. For the in-plane fracture, the fracture is shown in the XFEM model by the 1D line segment mesh superimposed on the 2D solution domain, while it is shown in the smeared cracking models by contours of the damage index in the first in-plane cracking direction. For the XFEM model, the plots showing the in-plane cracking are on the undisplaced mesh, while the contours of axial cracking are on the displaced mesh.

In both cases, the first cracks began to occur around 8 years. Because both models used the same randomized strength distributions, some of the cracks formed at the same locations. Fractures were driven by high tensile stresses in the regions with high fluence, as shown in Figure 17. In the XFEM model, once the first crack initiated on the upper right surface of the model, it propagated relatively quickly, while the smeared cracking model predicted the propagation of two major cracks on opposing sides of the model in a nearly

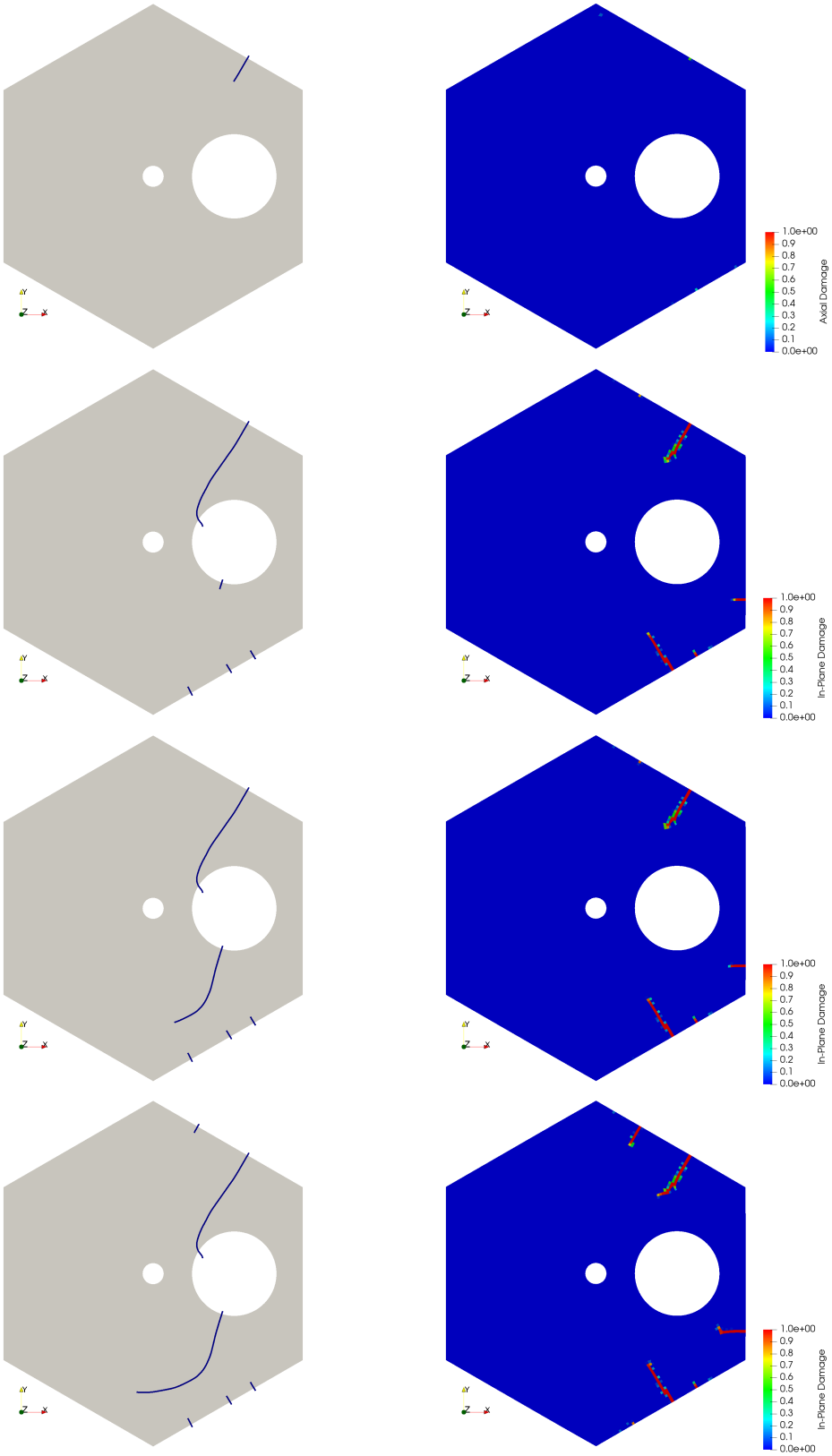

Figure 19: Comparison of in-plane fracture computed by 2D planar (left) XFEM and (right) smeared cracking models. Results are shown after (from top to bottom) 8.8, 21.8, 22.6, and 30 years.

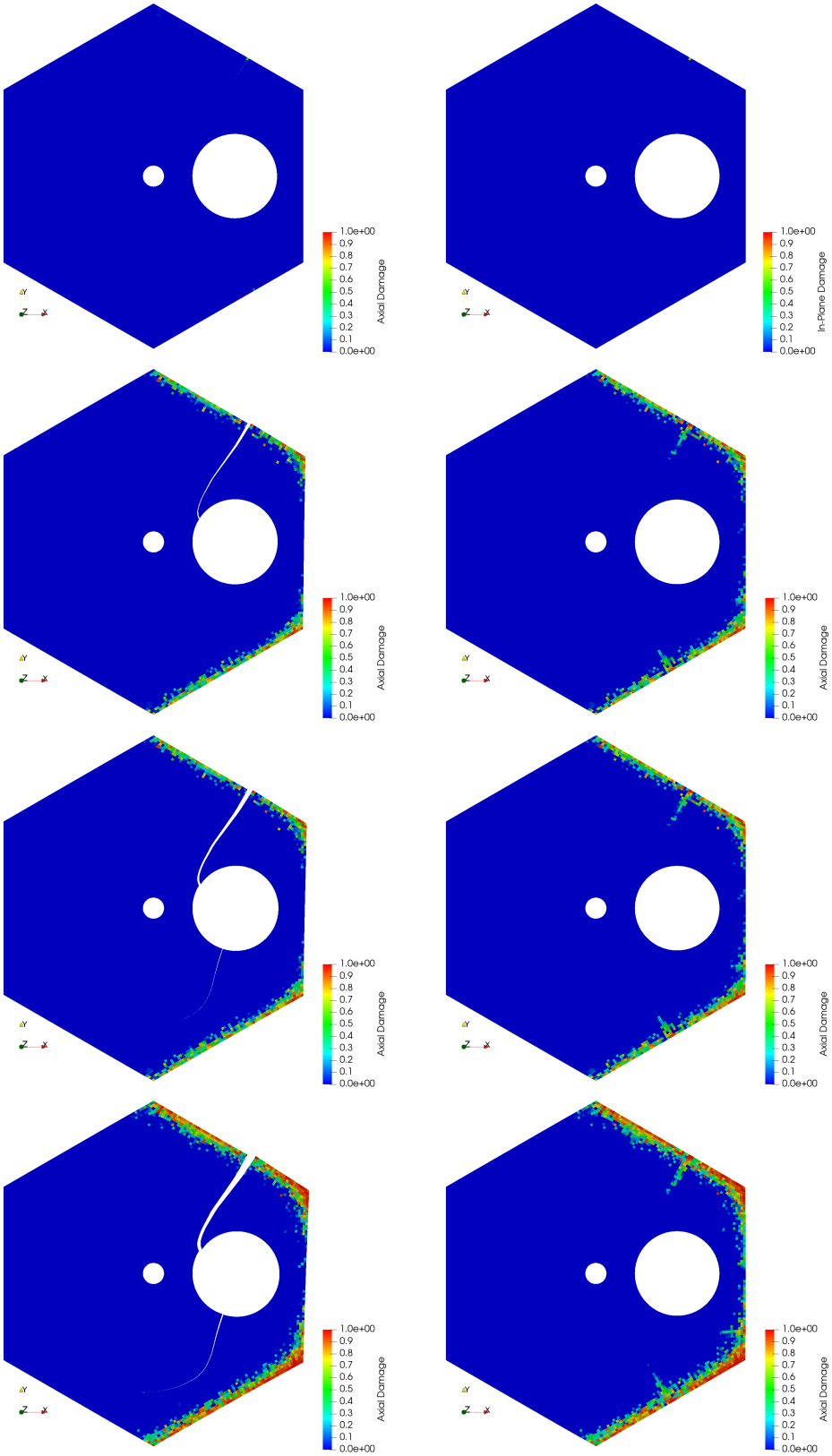

Figure 20: Comparison of axial fracture computed by 2D planar (left) XFEM and (right) smeared cracking models. Results are shown after (from top to bottom) 8.8, 21.8, 22.6, and 30 years.

symmetric fashion. Either of these scenarios is plausible, and the behavior could be affected significantly by the response of the models to the randomized strength distributions. In the case of the XFEM model, only fracture nucleation is affected by the randomized strength, while in the smeared cracking model, both fracture initiation and growth are affected by the local values of the randomized strength. It is notable that the smeared cracking model shows highly localized cracks on bands with widths of one or two finite elements. It is possible that the smeared cracking model did not predict localization in a single major crack in the way that the XFEM model did because the smeared cracking model did not allow a full loss of strength across the crack. Element deletion is commonly used to mitigate this, which could be explored with further work.

Once the single major crack predicted by the XFEM model propagates to the control rod hole, the stress state in the block is altered significantly, with elevated stresses on the interior of that hole that eventually result in a second major crack nucleating and growing across the other half of the block. The first crack experiences significant opening because the region with high shrinkage around the rightmost three faces is able to cause global bending, which is what contributes to the high stresses in the control rod hole.

It is also notable that the extents of axial cracking predicted by both the XFEM and smeared cracking models is similar and is quite significant but does not extend deeply into the block. Some interaction between the axial cracking and in-plane cracking is observed in the smeared cracking model but not in the XFEM model.

In the XFEM simulation images, it is evident that the first crack continued to grow past the free surface for a short distance. In addition, the initially nucleated cracks extend out of the solution domain. These are both artifacts of the XFEM cutting mesh implementation that will be addressed with future developments.

Figure 21 shows the damage predicted by the 3D smeared cracking model. In these images, the base model is shown translucent and damage is indicated by the damage in the first cracking direction. Elements with nonzero damage are filtered and shown superimposed on the base model. This allows for better visualization of the extent to which cracks penetrate the interior of the domain. For the most part, these results are consistent with those of the 2D smeared cracking model. Cracking in the $x - y$ plane occurs at locations and extents generally consistent with those of the 2D model. These cracks tend to penetrate more deeply into the interior of the body near the top and bottom surfaces in the 3D model than in the interior. Figure 22 shows a view from the top of the 3D model, highlighting the extent to which axial cracks penetrate in to the body. The comparable result for the 2D model is shown alongside the 3D result. While the 3D model predicts deeper penetration of cracks, the deepest cracks were spaced fairly far apart.

While there are certainly some discrepancies between the fracture patterns predicted by these models, there is a remarkable level of agreement between them in many respects. Each of these modeling approaches has its strengths, and it is important to provide multiple methods for addressing different aspects of fracture mechanics problems and to note that these simulation results are only being compared against other simulations. While doing this is a useful exercise, it is critical to validate numerical models against experimental data, which is an important area of future work.

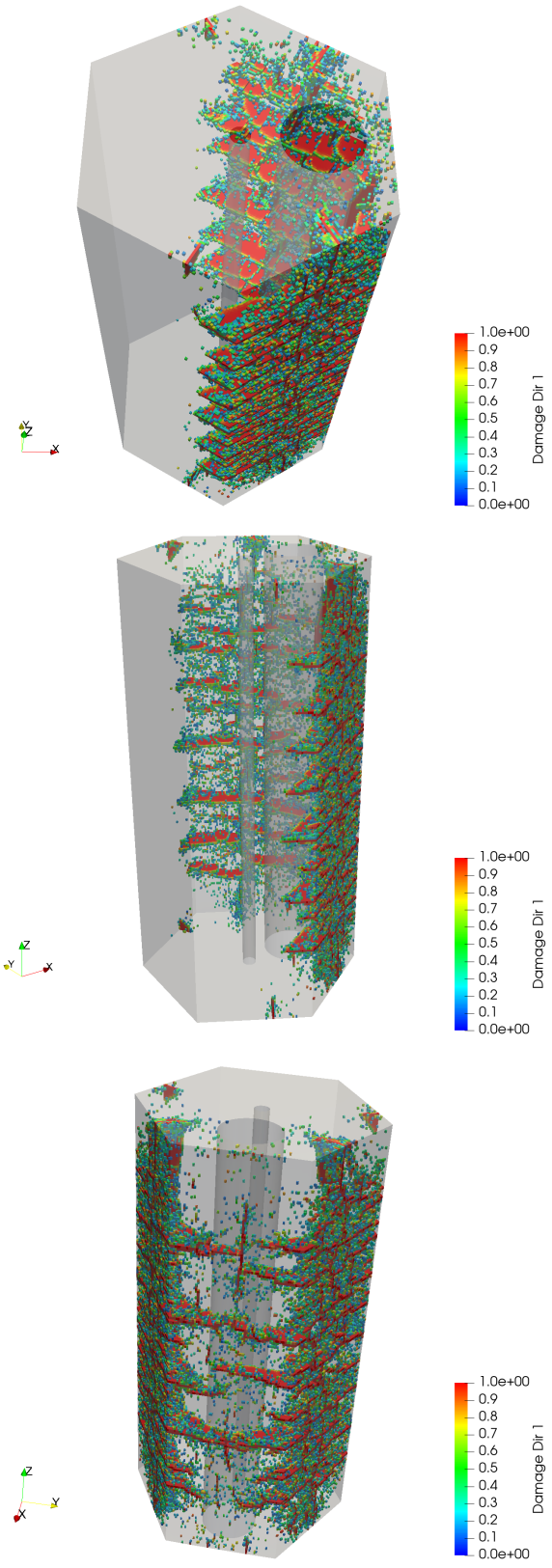

Figure 21: Damage predicted by the 3D smeared cracking model after 30 years from three different viewpoints.

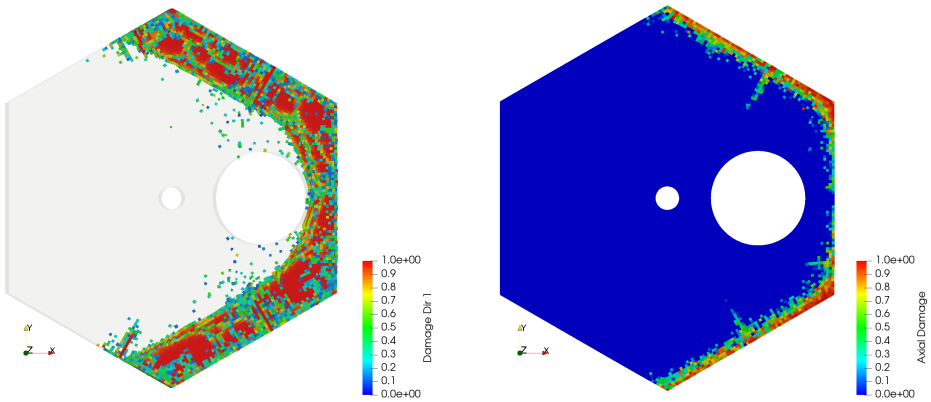

Figure 22: Comparison of axial fracture computed by (left) the 3D smeared cracking model and (right) the 2D smeared cracking model after 30 years. To allow better visualization of the behavior in the interior of the domain, the 3D model shows a view from the top with parallel projection, with only elements with nonzero damage shown superimposed on a base translucent model.

6 SUMMARY AND FUTURE WORK

This report details recent developments in MOOSE, Grizzly, and Blackbear to model material failure in general, with the specific objective of developing a capability to model fracture initiation and propagation in graphite components. The most significant development was enhancing the XFEM 2D cutting algorithms to capture the geometry of the cut surface through a separate cutting mesh that is able to capture crack growth using fracture integrals. This significantly improves the accuracy and robustness of the 2D cutting algorithms and makes them consistent with the procedures used in the 3D XFEM fracture propagation algorithm. We also continued the development of nonlinear models for quasibrittle materials in Blackbear that were initially developed for concrete but, after reparameterization, are also applicable to graphite. We also implemented several mechanical and thermal models for common graphite grades with nuclear applications.

The nonlinear model for quasibrittle material was applied to improve the predictions of stresses in a splitting disc test. The developments in fracture models and in material models for graphite were combined in a demonstration problem modeling irradiation swelling and fracture of a graphite VHTR reflector brick. We performed full 3D simulations using smeared cracking models on these bricks and smaller-scale simulations capturing fracture under 2D plane strain conditions using both XFEM and smeared cracking. After accounting for the mesh dependence of the fracture energy, the smeared cracking and XFEM discrete fracture simulations showed similar fracture features. Similar amounts of radial cracking and regions containing large amounts of axial cracking were observed in the 2D and 3D models. Several of the radial cracks turned out to be nonplanar in the 3D model, which demonstrates the importance of full 3D simulations.

While the results presented here show significant progress in graphite fracture modeling, there are multiple areas where future work is warranted. The MOOSE XFEM module is still limited in its handling of crack branching and intersection. The underlying cutting algorithm can handle elements being cut multiple times, but the crack path definition code does not. The criteria for crack growth also need further development for short cracks that have just nucleated and for cracks that are propagating toward a free surface. In both of these cases, the fracture integrals currently used as growth criteria are inadequate. The use of nonlocal stresses in these cases may be a viable option. In addition, the XFEM simulations here were 2D, but the 3D algorithms for fracture propagation have seen limited application, and further testing and development is needed there. It is also important to note that the 3D algorithm has no nucleation capability yet, which would be modeled on the 2D capability.

The simulations demonstrated in this work did not delve into size effects in graphite fracture. These size effects are likely to become more apparent in loading scenarios where the stress localizes in several regions. These types of loading conditions are not adequately addressed by the current ASME standard, which groups together similarly stressed regions regardless of where they are located in the component. We expect the direct methods for fracture propagation to be useful in understanding size effects and that they could help inform the future development of consensus standards.

The graphite strength models used in this work did not account for the effects of irradiation and oxidation on graphite strength (e.g., [60][61]). Some oxidation models have already been developed in Grizzly, and connecting them to fracture models would be a logical future development.

Further work is also needed on the algorithms for randomizing the graphite strength. The current approach neglects any spatial correlation between sampled values, which we suspect is important. Implementing and testing an improved algorithm for strength randomization based on the Karhunen-Loueve expansion [62] could help address this.

Finally, it is important to emphasize that none of the simulations on graphite components shown here have been validated against experimental data, and until that is done, there will be limited confidence in these

models. It is also important to survey the available validation data, simulate components for which there is available data, and work with experimentalists to develop new tests that can be used for model validation.

REFERENCES

[1] *ASME Boiler and Pressure Vessel Code, Section III, Rules for Construction of Nuclear Facility Components, Division 5, High Temperature Reactors*. Number ASME BPVC.III.5-2021. ASME, 2021.

[2] Benjamin W. Spencer, William M. Hoffman, Sudipta Biswas, Wen Jiang, Alain Giorla, and Marie A. Backman. Grizzly and BlackBear: Structural component aging simulation codes. *Nuclear Technology*, 207(7):981–1003, April 2021. doi: 10.1080/00295450.2020.1868278.

[3] Alexander D. Lindsay, Derek R. Gaston, Cody J. Permann, Jason M. Miller, David Andrš, Andrew E. Slaughter, Fande Kong, Joshua Hansel, Robert W. Carlsen, Casey Icenhour, Logan Harbour, Guillaume L. Giudicelli, Roy H. Stogner, Peter German, Jacob Badger, Sudipta Biswas, Leora Chapuis, Christopher Green, Jason Hales, Tianchen Hu, Wen Jiang, Yeon Sang Jung, Christopher Matthews, Yinbin Miao, April Novak, John W. Peterson, Zachary M. Prince, Andrea Rovinelli, Sebastian Schunert, Daniel Schwen, Benjamin W. Spencer, Swetha Veeraraghavan, Antonio Recuero, Dewen Yushu, Yaqi Wang, Andy Wilkins, and Christopher Wong. 2.0 - MOOSE: Enabling massively parallel multiphysics simulation. *SoftwareX*, 20:101202, December 2022. doi: 10.1016/j.softx.2022.101202.

[4] Richard L. Williamson, Jason D. Hales, Stephen R. Novascone, Giovanni Pastore, Kyle A. Gamble, Benjamin W. Spencer, Wen Jiang, Stephanie A. Pitts, Albert Casagranda, Daniel Schwen, Adam X. Zabriskie, Aysenur Toptan, Russell Gardner, Christoper Matthews, Wenfeng Liu, and Hailong Chen. BISON: A flexible code for advanced simulation of the performance of multiple nuclear fuel forms. *Nuclear Technology*, 207(7):954–980, March 2021. doi: 10.1080/00295450.2020.1836940.

[5] Joseph Bass. Graphite degradation modeling and analysis. Technical Report TLR-RES/DE/REB-2022-11, INL/EXT-22-65240, Idaho National Laboratory, 2022. URL `https://adamswebsearch2.nrc.gov/webSearch2/main.jsp?AccessionNumber=ML22346A082`.

[6] Ke Shen, Suyuan Yu, and Feiyu Kang. The microstructure and texture of gilsocarbon graphite. *Carbon*, 153:428–437, November 2019. doi: 10.1016/j.carbon.2019.06.108.

[7] Anne A. Campbell, Andrew A. Wereszczak, Mary A. Snead, and Yutai Katoh. Understanding the effect of specimen size on the properties of fine-grain isotropic nuclear graphite for irradiation studies: Mechanical properties. *Journal of Nuclear Materials*, 576:154263, April 2023. doi: 10.1016/j.jnucmat.2023.154263.

[8] *Standard Guide for Categorization of Microstructural and Microtextural Features Observed in Optical Micrographs of Graphite*. Number D8075-16 (Reapproved 2021). ASTM International, 2021.

[9] Aysenur Toptan, Wen Jiang, Stephen Novascone, and Jason Hales. Matrix graphite material models in pebbles and compacts for bison. Technical Report INL/EXT-21-64643, Idaho National Laboratory, Idaho Falls, ID, September 2021.

[10] José David Arregui-Mena, Robert N. Worth, William Bodel, Benjamin März, Wenjing Li, Anne A. Campbell, Ercan Cakmak, Nidia Gallego, Cristian Contescu, and Philip D. Edmondson. Multiscale characterization and comparison of historical and modern nuclear graphite grades. *Materials Characterization*, 190:112047, August 2022. doi: 10.1016/j.matchar.2022.112047.

[11] J. David Arregui-Mena, Philip D. Edmondson, David Cullen, Samara Levine, Cristian Contescu, Yutai Katoh, and Nidia Gallego. Microstructural characterization of the CGB graphite grade from the molten salt reactor experiment. *Journal of Nuclear Materials*, 582:154421, August 2023. doi: 10.1016/j.jnucmat.2023.154421.

[12] Kairos Power. Graphite material qualification for the Kairos Power fluoride salt-cooled high temperature reactor Topical report. Technical report, Kairos Power, 2022. URL https://www.nrc.gov/docs/ML2213/ML22132A205.pdf.

[13] R. Moskovic, P.J. Heard, P.E.J. Flewitt, and M.R. Wootton. Overview of strength, crack propagation and fracture of nuclear reactor moderator graphite. *Nuclear Engineering and Design*, 263:431–442, October 2013. doi: 10.1016/j.nucengdes.2013.05.011.

[14] P.J. Heard, M.R. Wootton, R. Moskovic, and P.E.J. Flewitt. Deformation and fracture of irradiated polygranular pile grade a reactor core graphite. *Journal of Nuclear Materials*, 418(1-3):223–232, November 2011. doi: 10.1016/j.jnucmat.2011.07.003.

[15] Martin Metcalfe. Damage tolerance in the graphite cores of UK power reactors and implications for new build. *Nuclear Engineering and Design*, 406:112237, May 2023. doi: 10.1016/j.nucengdes.2023.112237.

[16] Z. P. Bažant and Jaime Planas. *Fracture and size effect in concrete and other quasibrittle materials*. New directions in civil engineering. CRC Press, Boca Raton, 1998. ISBN 084938284X.

[17] Waloddi Weibull. The phenomenon of rupture in solids. *Proceedings of the Royal Swedish Institute of Engineering Research*, 153:1–45, 1939.

[18] Waloddi Weibull. A statistical distribution function of wide applicability. *Journal of applied mechanics*, 1951. URL https://hal.science/hal-03112318/document.

[19] Frank W. Zok. On weakest link theory and Weibull statistics. *Journal of the American Ceramic Society*, 100(4):1265–1268, April 2017. doi: 10.1111/jace.14665.

[20] Noel N. Nemeth and Robert L. Bratton. Overview of statistical models of fracture for nonirradiated nuclear-graphite components. *Nuclear Engineering and Design*, 240(1):1–29, January 2010. doi: 10.1016/j.nucengdes.2009.10.002.

[21] Noel Nemeth, Andrew Walker, Eric Baker, Pappu Murthy, and Robert Bratton. Large-scale weibull analysis of h-451 nuclear-grade graphite rupture strength. *Carbon*, 58:208–225, July 2013. doi: 10.1016/j.carbon.2013.02.054.

[22] Michael P. Hindley, Mark N. Mitchell, Christiaan Erasmus, Ross McMurtry, Thorsten H. Becker, Deborah C. Blaine, and Albert A. Groenwold. A numerical stress based approach for predicting failure in NBG-18 nuclear graphite components with verification problems. *Journal of Nuclear Materials*, 436(1-3):175–184, May 2013. doi: 10.1016/j.jnucmat.2012.10.030.

[23] Michael P. Hindley. *Next generation high-temperature gas reactors: A failure methodology for the design of nuclear graphite components*. PhD thesis, Sellenbosch University, 2015. URL http://hdl.handle.net/10019.1/97071.

[24] Andrea Nicolas, Mark Messner, and T. Sham. Preliminary design analysis workflow for Division 5 HHA-3200 requirements for graphite core components. Technical report, August 2020.

[25] José David Arregui-Mena, Robert N Worth, Graham Hall, Philip D Edmondson, Alain B Giorla, and Timothy D Burchell. A review of finite element method models for nuclear graphite applications. *Arch. Comput. Methods Eng.*, 27(1):331–350, January 2020. doi: 10.1007/s11831-018-09310-y.

[26] Z. Zou, S.L. Fok, B.J. Marsden, and S.O. Oyadiji. Numerical simulation of strength test on graphite moderator bricks using a continuum damage mechanics model. *Engineering Fracture Mechanics*, 73 (3):318–330, February 2006. doi: 10.1016/j.engfracmech.2005.08.002.

[27] M. Wadsworth, S.T. Kyaw, and W. Sun. Finite element modelling of the effect of temperature and neutron dose on the fracture behaviour of nuclear reactor graphite bricks. *Nuclear Engineering and Design*, 280:1–7, December 2014. doi: 10.1016/j.nucengdes.2014.10.009.

[28] S.T. Kyaw, D.W.J. Tanner, A.A. Becker, W. Sun, and D.K.L. Tsang. Modelling crack growth within graphite bricks due to irradiation and radiolytic oxidation. *Procedia Materials Science*, 3:39–44, 2014. doi: 10.1016/j.mspro.2014.06.009.

[29] L Kaczmarczyk. Fracture propagation in nuclear graphite. In *Proceedings of the 10th International Conference on Fracture Mechanics of Concrete and Concrete Structures*. IA-FraMCoS, June 2019. doi: 10.21012/fc10.235469.

[30] Costy Kodsi. *Computational framework for fracture of graphite bricks in an AGR core*. PhD thesis, University of Glasgow, 2017. URL `http://theses.gla.ac.uk/8084/`.

[31] Łukasz Kaczmarczyk, Zahur Ullach, Karol Lewandowski, and Chris Pearce. MoFEM-FractureModule-Module-v0.4.1, 2017.

[32] T. Crump, A.P. Jivkov, P. Mummery, G. Ferté, and V.X. Tran. Analysis of dynamic fracture and fragmentation of graphite bricks by combined XFEM and cohesive zone approach. *International Journal of Pressure Vessels and Piping*, 171:117–124, March 2019. doi: 10.1016/j.ijpvp.2019.02.013.

[33] Z Zou, SL Fok, SO Oyadiji, and BJ Marsden. Failure predictions for nuclear graphite using a continuum damage mechanics model. *Journal of Nuclear Materials*, 324(2-3):116–124, 2004. doi: 10.1016/j.jnucmat.2003.09.005.

[34] ST Kyaw, DWJ Tanner, AA Becker, Winnie Sun, and DKL Tsang. Modelling crack growth within graphite bricks due to irradiation and radiolytic oxidation. *Procedia materials science*, 3:39–44, 2014.

[35] M Wadsworth, Si Thu Kyaw, and Wei Sun. Finite element modelling of the effect of temperature and neutron dose on the fracture behaviour of nuclear reactor graphite bricks. *Nuclear Engineering and Design*, 280:1–7, 2014.

[36] Gyanender Singh, Alex Fok, and Susan Mantell. Failure Predictions for Graphite Reflector Bricks in the Very High Temperature Reactor with the Prismatic Core Design. *Nuclear Engineering and Design*, 317:190–198, June 2017. ISSN 00295493. doi: 10.1016/j.nucengdes.2017.03.037.

[37] Gyanender Singh. Explicit crack modeling based approach for structural integrity assessment of brittle and quasi-brittle structures. 2015.

[38] Łukasz Kaczmarczyk, Zahur Ullah, Karol Lewandowski, Xuan Meng, Xiao-Yi Zhou, Ignatios Athanasiadis, Hoang Nguyen, Christophe-Alexandre Chalons-Mouriesse, Euan J Richardson, Euan Miur, et al. Mofem: An open source, parallel finite element library. *Journal of Open Source Software*, 5(45):1441, 2020.

[39] Y.R. Rashid. Ultimate strength analysis of prestressed concrete pressure vessels. *Nuclear Engineering and Design*, 7(4):334–344, April 1968. ISSN 00295493. doi: 10.1016/0029-5493(68)90066-6.

[40] Y.R. Rashid. Mathematical modeling and analysis of fuel rods. *Nuclear Engineering and Design*, 29 (1):22–32, November 1974. ISSN 00295493. doi: 10.1016/0029-5493(74)90095-8.

[41] O.E. Strack, R.B. Leavy, and R.M. Brannon. Aleatory uncertainty and scale effects in computational damage models for failure and fragmentation. *International Journal for Numerical Methods in Engineering*, 102(3-4):468–495, April 2015. ISSN 00295981. doi: 10.1002/nme.4699.

[42] T. Belytschko and T. Black. Elastic crack growth in finite elements with minimal remeshing. *International Journal for Numerical Methods in Engineering*, 45(5):601–620, June 1999. ISSN 0029-5981, 1097-0207. doi: 10.1002/(SICI)1097-0207(19990620)45:5<601::AID-NME598>3.0.CO;2-S.

[43] A. Hansbo and P. Hansbo. A finite element method for the simulation of strong and weak discontinuities in solid mechanics. *Computer Methods in Applied Mechanics and Engineering*, 193(33-35):3523–3540, Aug 2004. doi: 10.1016/j.cma.2003.12.041.

[44] Wen Jiang, Benjamin W. Spencer, and John E. Dolbow. Ceramic nuclear fuel fracture modeling with the extended finite element method. *Engineering Fracture Mechanics*, 223:106713, January 2020. ISSN 00137944. doi: 10.1016/j.engfracmech.2019.106713.

[45] Benjamin W. Spencer, William M. Hoffman, and Wen Jiang. Weight function procedure for reduced order fracture analysis of arbitrary flaws in cylindrical pressure vessels. *International Journal of Pressure Vessels and Piping*, 200:104784, August 2022. doi: 10.1016/j.ijpvp.2022.104784.

[46] Louis Bailly-Salins, Léo Borrel, Wen Jiang, Benjamin W. Spencer, Koroush Shirvan, and Adrien Couet. Modeling of high-temperature corrosion of zirconium alloys using the eXtended finite element method (X-FEM). *Corrosion Science*, 189:109603, August 2021. doi: 10.1016/j.corsci.2021.109603.

[47] B. W. Spencer, J. H. Ke, S. Biswas, W. M. Hoffman, A. M. Recuero, D. Schwen, L. B. Munday, S. L. Dhulipala, S. A. Pitts, A. Casagranda, L. Liu, and J. He. Summary of structural material modeling development for the NEAMS program in fiscal year 2020. Technical Report INL/EXT-20-60192, Idaho National Laboratory, October 2020.

[48] Jacky Mazars. *Application de la mécanique de l'endommagement au comportement non linéaire et à la rupture du béton de structure*. PhD thesis, Université Paris 6, France, 1984.

[49] J. Mazars and G. Pijaudier-Cabot. Continuum Damage Theory—Application to Concrete. *Journal of Engineering Mechanics*, 115:345–365, February 1989. doi: 10.1061/(ASCE)0733-9399(1989)115:2(345).

[50] Jeeho Lee and Gregory L. Fenves. Plastic-Damage Model for Cyclic Loading of Concrete Structures. *Journal of Engineering Mechanics*, 124(8):892–900, August 1998. doi: 10.1061/(ASCE)0733-9399(1998)124:8(892).

[51] R. Ballarini, B. Gencturk, A. Jain, H. Aryan, Y. Xi, M. Abdelrahman, and B. Spencer. Multiple degradation mechanisms in reinforced concrete structures, modeling and risk analysis. Technical Report INL/EXT-20-57095, Idaho National Laboratory, February 2020.

[52] *Standard Test Methods for Tension Testing of Carbon and Graphite Mechanical Materials*. Number C565-15 (Reapproved 2021). ASTM International, 2021.

[53] *Standard Test Method for Tensile Strength Estimate by Disc Compression of Manufactured Graphite*. Number D8289-20. ASTM International, 2020.

[54] Generation IV Interational Forum. Technology roadmap update for Generation IV nuclear energy systems. Technical report, OECD Nuclear Energy Agency, 2014. URL https://www.gen-4.org/gif/jcms/c_60729/technology-roadmap-update-2013.

[55] Gen-IV International Forum - Very High Temperature Reactor. https://www.gen-4.org/gif/jcms/c_42153/very-high-temperature-reactor-vhtr. Accessed: 2023-06-26.

[56] Robert L. Bratton. Modeling mechanical behavior of a prismatic replaceable reflector block. Technical Report INL/EXT-09-15868, Idaho National Laboratory, April 2009.

[57] J Ortensi, G Strydom, MA Pope, A Bingham, H Gougar, RS Sen, V Seker, T Downar, C Ellis, A Baxter, et al. Benchmark of the modular high-temperature gas-cooled reactor (mhtgr)-350 mw core design volumes i and ii, 2018.

[58] F. H. Ho. Graphite design handbook. Technical Report DOE-HTGR-88111, General Atomics, 1988.

[59] G.B. Engle. Assessment of grade H-451 graphite for replaceable fuel and reflector elements in HTGR. Technical report, December 1977.

[60] Austin C. Matthews, Joshua J. Kane, W. David Swank, and William E. Windes. Nuclear graphite strength degradation under varying oxidizing conditions. *Nuclear Engineering and Design*, 379: 111245, August 2021. doi: 10.1016/j.nucengdes.2021.111245.

[61] Joshua J. Kane, Cristian I. Contescu, Rebecca E. Smith, Gerhard Strydom, and William E. Windes. Understanding the reaction of nuclear graphite with molecular oxygen: Kinetics, transport, and structural evolution. *Journal of Nuclear Materials*, 493:343–367, September 2017. doi: 10.1016/j.jnucmat.2017.06.001.

[62] Tianchen Hu, Johann Guilleminot, and John E. Dolbow. A phase-field model of fracture with frictionless contact and random fracture properties: Application to thin-film fracture and soil desiccation. *Computer Methods in Applied Mechanics and Engineering*, 368:113106, August 2020. doi: 10.1016/j.cma.2020.113106.